Cell Reports
Medicine

Article

Outer radial glia promotes white matter regeneration after neonatal brain injury

Graphical abstract

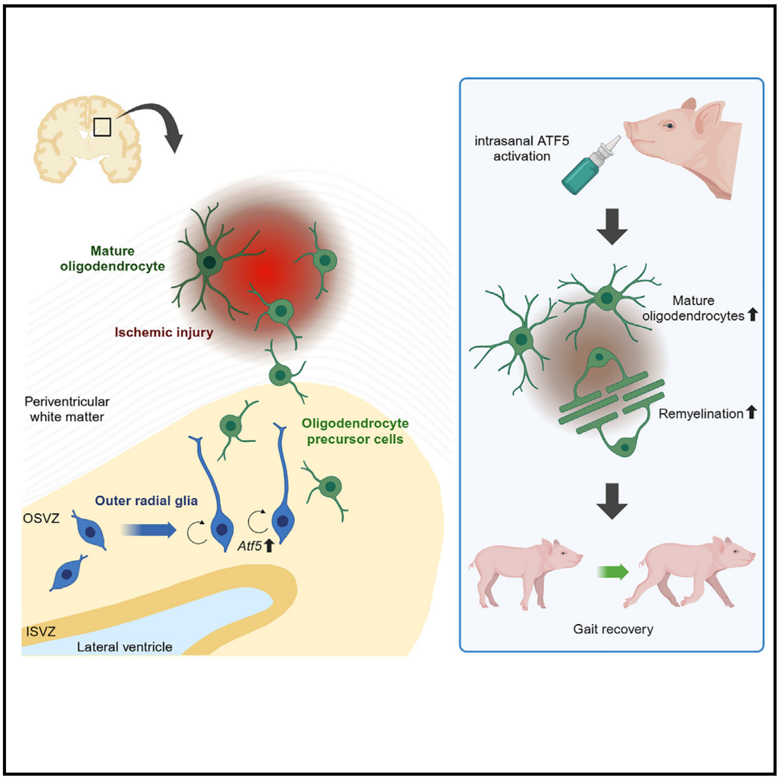

Authors

Hideo Jinnou, Lauren M. Rosko,
Satoshi Yamashita, ...,
Kazue Hashimoto-Torii,
Nobuyuki Ishibashi, Vittorio Gallo

Correspondence

nishibas@childrensnational.org (N.I.),
vittorio.gallo@seattlechildrens.org (V.G.)

In brief

Jinnou et al. demonstrate that postnatal oRG cells enhance their proliferative capacity after neonatal brain injury via upregulation of the ATF5 pathway, promoting the production of OSVZ-derived OPCs. Intranasal activation of ATF5 fosters oligodendrogenesis, leading to white matter regeneration and functional recovery.

Highlights

- oRG cells show increased proliferation after brain injury in infants and piglets
- Post-injury oRG proliferation boosts OPC production in the OSVZ
- The ATF5 pathway promotes cell proliferation and anti-apoptosis in oRG cells
- Intranasal ATF5 activation improves white matter injury and behavioral outcomes

Jinnou et al., 2025, Cell Reports Medicine *6*, 101986
March 18, 2025
https://doi.org/10.1016/j.xcrm.2025.101986

CellPress

Cell Reports Medicine

CellPress
OPEN ACCESS

Article

Outer radial glia promotes white matter regeneration after neonatal brain injury

Hideo Jinnou,[1,2] Lauren M. Rosko,[1] Satoshi Yamashita,[1] Soichiro Henmi,[1] Jaya Prasad,[1] Van K. Lam,[1] Artur Agaronyan,[3] Tsang-Wei Tu,[3] Yuka Imamura,[4] Kazuya Kuboyama,[5] Kazunobu Sawamoto,[5] Kazue Hashimoto-Torii,[1,6] Nobuyuki Ishibashi,[1,6,*] and Vittorio Gallo[1,6,7,8,9,*]

[1]Center for Neuroscience Research, Children's National Research Institute, Children's National Hospital, Washington, DC 20010, USA
[2]Department of Pediatrics and Neonatology, Nagoya City University, Graduate School of Medical Sciences, Nagoya 467-8601, Japan
[3]Molecular Imaging Laboratory, Department of Radiology, Howard University, Washington, DC 20059, USA
[4]Departments of Pharmacology and Biochemistry and Molecular Biology, Pennsylvania State University College of Medicine, Hershey, PA 17033, USA
[5]Department of Developmental and Regenerative Neurobiology, Institute of Brain Science, Nagoya City University Graduate School of Medical Sciences, Nagoya 467-8601, Japan
[6]Department of Pediatrics, Pharmacology and Physiology, George Washington University School of Medicine and Health Sciences, Washington, DC 20037, USA
[7]Seattle Children's Research Institute, Seattle Children's Hospital, Seattle, WA 98101, USA
[8]Department of Pediatrics, University of Washington, Seattle, WA 98105, USA
[9]Lead contact
*Correspondence: nishibas@childrensnational.org (N.I.), vittorio.gallo@seattlechildrens.org (V.G.)
https://doi.org/10.1016/j.xcrm.2025.101986

SUMMARY

The developing gyrencephalic brain contains a large population of neural stem cells in the ventricular zone and outer subventricular zone (OSVZ), the latter populated by outer radial glia (oRG). The role of oRG during postnatal development is not well understood. We show that oRG cells increase proliferative capacity and contribute to oligodendrocyte precursor cell (OPC) production following brain injury in human infants and neonatal piglets, whose brains resemble the human brain in structure and development. RNA sequencing revealed oRG-specific transcriptional responses to injury in piglets and showed that the activating transcription factor 5 (ATF5) pathway positively regulates oRG proliferation. Intranasal activation of ATF5 using salubrinal enhanced OSVZ-derived oligodendrogenesis in the injured periventricular white matter and improved functional recovery. These results reveal a key role for postnatal oRG in brain injury recovery and identify ATF5 as a potential therapeutic target for treating white matter injury in infants.

INTRODUCTION

The human cerebral cortex and white matter grow dramatically in size and complexity during the perinatal period.[1–3] This growth is attributed to an abundance of neural stem cells (NSCs) in the germinal zone and progenitor cells that populate the early postnatal brain.[4–6] While NSCs reside in the ventricular zone and subventricular zone (SVZ) adjacent to the lateral ventricle in the lissencephalic rodent forebrain, the developing human brain contains an additional cortical germinal region called the outer SVZ (OSVZ), populated with outer radial glia (oRG).[4,7] oRG cells act as an extra source of NSCs to produce not only cortical neurons but also oligodendrocyte precursor cells (OPCs), leading to the expansion of gray and white matter of the gyrencephalic cortex.[4,5] Although the developmental origin of the main cell types of the mammalian central nervous system and the role of specific germinal zones have been studied,[8] the role of oRG in the OSVZ after birth and in response to injury remains largely unknown.

Neonatal brain injury is commonly caused by hypoxia and ischemia during the perinatal period. An injury incidence of 1.5–3.0 per 1,000 live births results in approximately 1 million newborns who suffer from disabilities per year worldwide.[9,10] White matter is susceptible to ischemic insult as impaired myelination is the hallmark of neonatal white matter injury. This injury arises from two main pathogenetic mechanisms: (1) white matter necrosis that causes pan-cellular loss due to severe ischemia and (2) death and developmental delay of OPCs and pre-myelinating oligodendrocytes induced by milder insults.[11,12] Cerebral gray matter is also affected by hypoxia and ischemia, which induces neuronal loss and severe abnormalities in the maturation of dendritic arborizations.[12] Consequently, neonatal ischemia results in reductions of both cerebral white and gray matter volumes, leading to cerebral palsy, cognitive impairment, and a broad range of neurodevelopmental deficits later in life. Notably, periventricular white matter (PVWM) is a region of particular predilection for ischemic injury in neonates.[13,14] There are currently no available treatments or therapeutic interventions that promote regeneration of the injured white matter and functional recovery after ischemia.

In rodents, the postnatal SVZ is still an NSC niche capable of producing OPCs and neuroblasts. After neonatal brain injury,

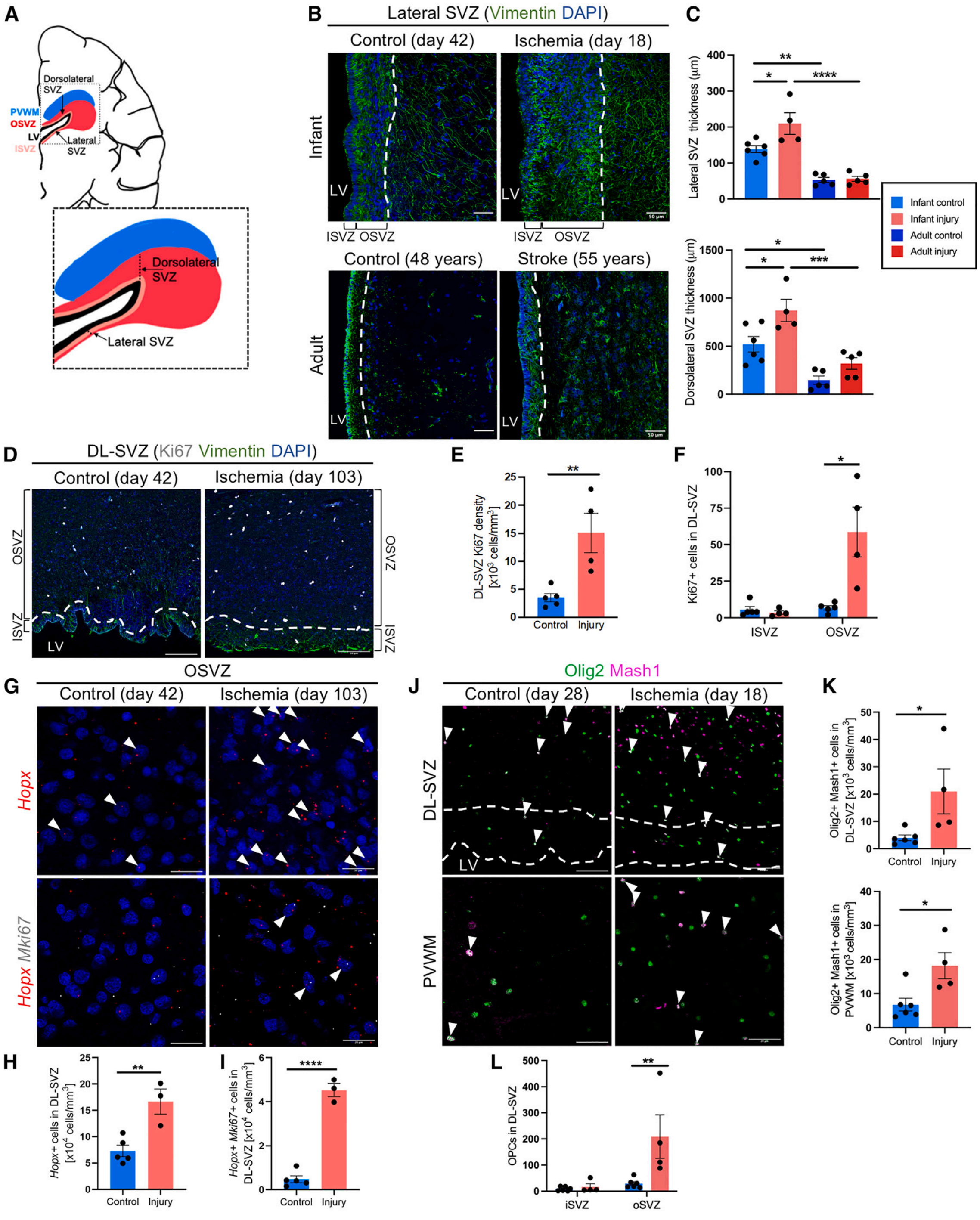

Figure 1. OSVZ enhances oRG proliferation and OPC production after ischemic brain injury in the human infant

(A) Illustration of the SVZ regions in the human brain.

(B) Coronal section of the L-SVZ of human infants and adults in control or ischemic injury groups, stained for vimentin (green) and DAPI (blue). Dashed lines indicate the border of the SVZ.

(C) Thickness of the L-SVZ (top) and DL-SVZ (bottom) (infant control *n* = 6, infant injury *n* = 4, adult control and injury *n* = 5, biological replicates).

(D) Coronal section of the DL-SVZ of human infants in control or ischemic injury groups, stained for Ki67 (white), vimentin (green), and DAPI (blue). Dashed lines indicate the border between the ISVZ and OSVZ.

(E) Density of Ki67$^+$ cells in the DL-SVZ of human infants (control *n* = 5, injury *n* = 4, biological replicates).

(F) The number of Ki67$^+$ cells in the ISVZ (left) and OSVZ (right) (control *n* = 5, injury *n* = 4, biological replicates).

(legend continued on next page)

the SVZ enhances its proliferative capacity and NSCs generate OPCs, which then migrate toward the lesion in the white matter to generate mature oligodendrocytes,[15–17] raising the possibility that the SVZ could also be a source for cellular replacement and white matter regeneration in human infants. However, significant differences exist between the human and rodent brain, including the much-enlarged gyrencephalic cortex, the different size and developmental trajectory of the white matter, and the more complex and multilayered cytoarchitecture of the SVZ in humans.[2,3,7,18,19] Significant cellular proliferation has been recognized in the human SVZ during the first few months after birth,[20] indicating that the regenerative capacity of the SVZ may be conserved in the human infant. However, obvious ethical and technical difficulties to obtain human tissues during the early postnatal period prevent detailed cellular and molecular analyses aimed at identifying the response and role of the human SVZ in neonatal brain injury. These obstacles can at least be partially overcome by analyzing the consequences of neonatal injury in the developing piglet brain, which shares structural and developmental characteristics with its human counterpart.[21–24] Our previous study using fractional anisotropy (FA) from diffusion tensor imaging (DTI) showed that piglet white matter at 3 weeks postnatal reflects human white matter from 41 to 53 weeks post conception,[25] suggesting that white matter in a 2-week-old piglet can model neonatal white matter in humans.

The piglet is recognized as a powerful model suitable for developmental studies and to investigate the effects of pathological conditions in the human infant brain. In the present study, we analyzed neonatal brain injury in humans and piglets. We demonstrate that ischemic brain injury results in enhanced cell proliferation and expansion of oRGs and OPCs in the OSVZ of human infants. These responses are reproduced in a neonatal piglet model of ischemic PVWM injury. Our RNA sequencing (RNA-seq) analysis shows that an anti-apoptotic pathway downstream of *Mcl1* regulates the proliferative capacity of oRG cells after brain injury via upregulation of *Atf5*. Through an integrated multi-disciplinary approach, we demonstrate that intranasal administration of a drug that activates the activating transcription factor 5 (ATF5) pathway promotes OSVZ-derived oligodendrogenesis and subsequent remyelination in the injured PVWM. Notably, ATF5 modulation with salubrinal, a drug shown to be cytoprotective during endoplasmic reticulum stress,[26] also improves microstructural alterations in the PVWM and impairment of gait behaviors resulting from ischemic PVWM injury. Our study not only reveals the functional role of oRG in the OSVZ in white matter regeneration in infants with neonatal brain injury but also identifies molecular mechanisms that regulate this regenerative process in the large mammalian and human brain.

RESULTS

OSVZ enhances oRG proliferation and OPC production after ischemic brain injury in the human infant

While proliferation of the lateral SVZ has been observed in the early postnatal human,[20] little is known about the response of the human infant SVZ to brain injury. To analyze the cellular changes of the human SVZ resulting from age and injury, we first analyzed human brain tissues obtained from early infants (0–142 days after birth) and adults with or without ischemia (Table S1). Ischemia, the most common cause of neonatal cerebral PVWM injury and adult brain injury,[27–29] was confirmed in all cases of the injury groups. Consistent with previous findings,[30] we also confirmed that ischemic injury caused a decrease in the density of CC1$^+$ mature oligodendrocytes in the PVWM, as compared with controls (Figures S1A and S1B). We observed a reduction in total cumulative length of processes per microglia suggesting increased activation of these cells after injury (Figures S1C and S1D). However, we did not observe changes in astrocytic intensity as a result of injury (Figure S1E).

Regional differences in structural and cellular properties have been identified in the human SVZ.[31] Therefore, we divided the human SVZ into dorsolateral (DL) and lateral (L) regions, based on previous studies in rodents and piglets (Figure 1A).[24,32] In both DL- and L-SVZ, the thickness of the SVZ was larger in infants than that in adults (Figures 1B and 1C). Furthermore, the SVZ thickness was increased after ischemic injury in infants, but not in adults (Figures 1B and 1C), suggesting significant cellular reactivity of the human infant SVZ to brain injury. Consistent with these structural changes, the density of Ki67$^+$ proliferative cells was significantly increased in both DL- and L-SVZ after ischemic injury in the infant brains (Figures 1D, 1E, S1F, and S1G). The SVZ in human and other gyrencephalic mammals is also subdivided into discrete cytoarchitectural regions called the inner SVZ (ISVZ) and OSVZ.[4,33] The sharp boundary between the ISVZ and OSVZ was identified based on cell density, as previously described.[33] When the DL-SVZ was further divided into these two regions, we found that the increase in cell proliferation occurred in the OSVZ, but not the ISVZ (Figure 1F).

It has been well documented that oRG cells actively proliferate as NSCs to accelerate the expansion of the gyrencephalic cortex during the early fetal period.[4,5] We found that, in normal development, the density of cells expressing the oRG marker *Hopx*[34] decreased with age within the first few months after birth (Figure S1H). In contrast to the embryonic phase, most of the postnatal oRG cells were not proliferative during normal development (6.2% ± 0.9% of *Hopx*$^+$ cells, Figure S1I). On the other hand, the densities of both total and proliferating oRG

(G) Coronal section of the DL-OSVZ of human infants in control or ischemic injury groups. Arrowheads indicate the presence of mRNA puncta of *Hopx* (top) and *Hopx* with *Mki67* (bottom).

(H and I) The percentage of cells that contain *Hopx* (H) or *Hopx*$^+$*Mki67*$^+$ (I) mRNA puncta in the DL-SVZ (control n = 5, injury n = 3, biological replicates).

(J) Coronal section of the DL-SVZ (top) and PVWM (bottom) of human infants in control or ischemic injury groups, stained for Olig2 (green) and Mash1 (magenta). Dashed lines indicate the borders between the lateral ventricle and SVZ and between the ISVZ and OSVZ. Arrowheads indicate colocalization of Olig2 and Mash1.

(K) Density of Olig2$^+$Mash1$^+$ cells in the DL-SVZ (top) and PVWM (bottom) of human infants (control n = 6, injury n = 4, biological replicates).

(L) The number of Olig2$^+$Mash$^+$ OPCs in the ISVZ (left) and OSVZ (right) (control n = 6, injury n = 4, biological replicates).

Data are represented as mean ± SEM. Statistical analyses: (C) one-way ANOVA with Tukey's multiple comparisons test; (E, H and I, K) unpaired t test; (F, L) two-way ANOVA with Sidak's multiple comparisons test. *$p < 0.05$, **$p < 0.01$, ***$p < 0.001$, ****$p < 0.0001$. Scale bar: (B) 50 μm, (D) 20 μm, (G) 20 μm, and (J) 20 μm. See also Figure S1 and Table S1.

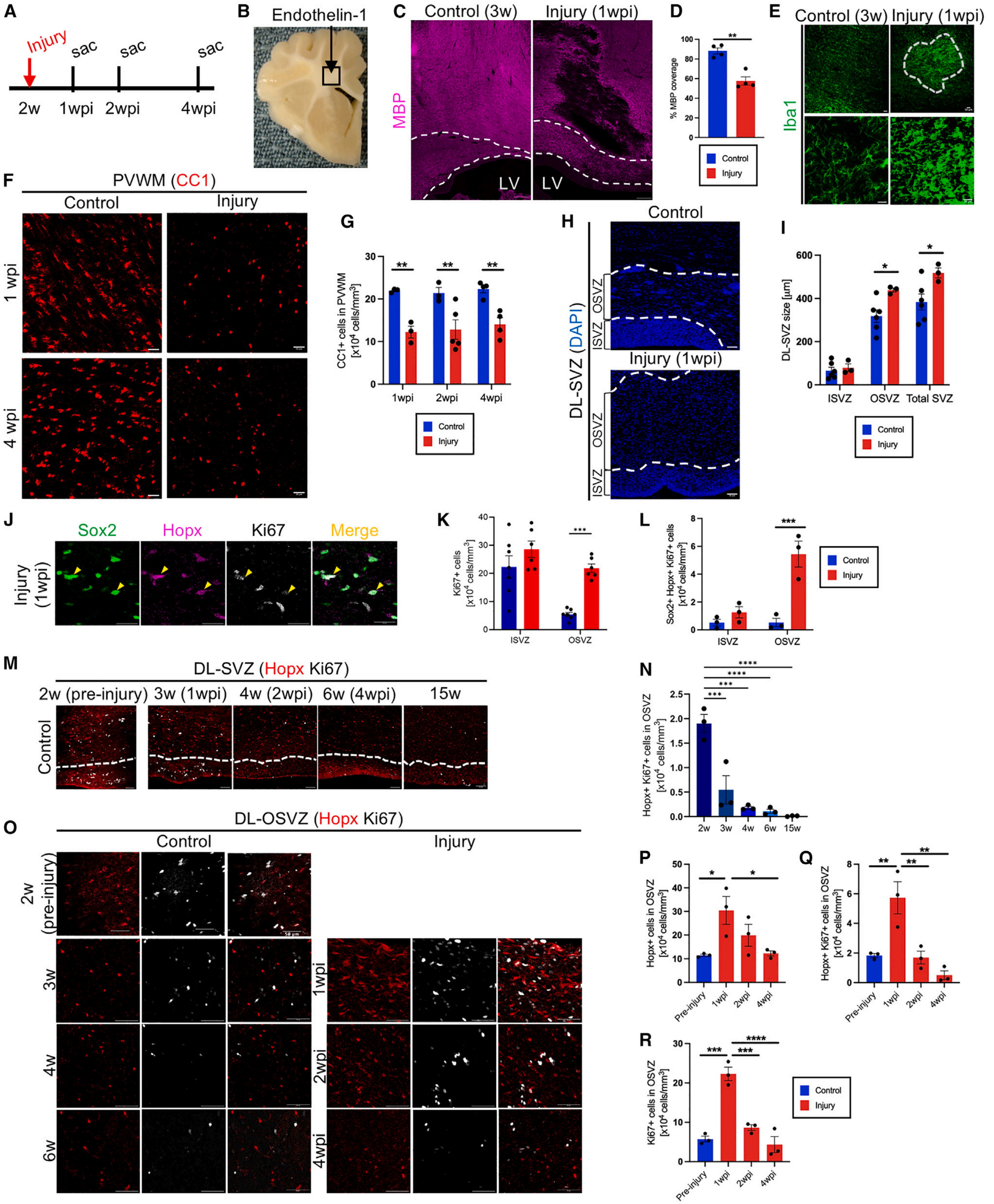

(legend on next page)

cells were significantly increased after ischemia, as compared to controls (Figures 1G–1I). Consistent with these findings, the percentage of proliferative oRG cells was increased after ischemic injury (Figure S1I). oRGs in the fetal OSVZ have a long basal process to support neuronal migration as a scaffold.[35] Our analysis found that postnatal Vimentin$^+$ oRG cells display short and branched processes in normal development. Notably, we observed a large increase in postnatal oRG cells with elongated processes after ischemic injury (Figures S1J–S1L), which is similar to the morphological characteristic seen in oRG cells during the embryonic period.[4,36]

In addition to the response of oRG cells, the density of Olig2$^+$Mash1$^+$ OPCs[16,23] was also significantly increased after ischemia in both the DL-SVZ and its surrounding PVWM of the human infant brain (Figures 1J and 1K). During the fetal period, OPCs can be produced by oRG cells in the OSVZ.[5] Indeed, OPCs within the postnatal human SVZ were largely located in the OSVZ, but not in the ISVZ (Figure 1L). Aligned with the OPC expansion observed in the OSVZ and PVWM, the density of Olig2$^+$ oligodendrocytes in these two regions was also higher in the injury group compared to controls (Figures S1M and S1N). These results suggest that the human OSVZ during the early infant period has the potential to promote oligodendrogenesis after ischemic injury.

oRG cells increase their proliferative capacity after piglet brain injury

In order to replicate ischemic white mater injury occurring in the human infant, the potent vasoconstrictor endothelin-1 was injected into the right PVWM of 2-week-old piglets (Figures 2A and 2B). We observed a reduction in myelin basic protein (MBP) expression and a persistent decrease in CC1$^+$ oligodendrocytes in the PVWM after endothelin-1-induced ischemic insults (Figures 2C, 2D, 2F, and 2G). We also observed an increase in Iba1$^+$ activation shown by a reduction in the cumulative length of processes per microglia and reduced branch points per microglia (Figures 2E and S2A). In this demyelination model, we did not observe significant axonal damage determined by the expression of neurofilament 200 and non-phosphorylated neurofilament (SMI-32) (Figures S2B–S2D). Consistent with our findings in the human infant SVZ (Figures 1B and 1C), the DL-SVZ was expanded after injury in the piglet brain (Figure 2H). Notably, the increase in overall SVZ thickness was due to expansion of the OSVZ, but not of the ISVZ (Figure 2I). Although ischemic PVWM injury did not induce significant cellular proliferation within the ISVZ, the Ki67$^+$ cell density in the OSVZ was significantly increased after injury (Figures 2J and 2K). Similarly, the densities of both Sox2$^+$ NSCs and proliferating NSCs were significantly higher in the OSVZ after injury, but not in the ISVZ (Figures 2J, 2L, and S2E–S2G). Consistent with our findings in the human infant, the postnatal piglet brain also showed an age-dependent decline of oRG cell proliferation (Figures 2M and 2N). However, ischemic PVWM injury induced a significant increase in oRG cell proliferation (Figures 2L and S2H). When the time course of cell proliferation was analyzed, the total number of oRG cells and their proliferation in the OSVZ region peaked at 1 week post injury (wpi) (Figures 2O–2R). At this time point, approximately 20% of oRG cells were proliferative (Figure S2H). Finally, piglet oRG cells also extended their processes in response to brain injury (Figures S2I–S2K) as observed in human infant oRG cells (Figures S1J–S1L). Taken together, in addition to structural and developmental similarities, ischemic injury in neonatal piglets recapitulates the injury-induced response of oRG cells in the human infant.

Brain injury enhances the production of OSVZ OPCs, which migrate to the PVWM lesion to generate mature oligodendrocytes

Since the human infant brain displayed injury-induced OPC expansion in the SVZ (Figures 1J–1L), we next analyzed the response of OPCs in the piglet injury model. Consistent with our findings in the human infant, the ischemic injury induced an increase in OPC density in both the DL-SVZ and in the injured PVWM region of the piglet. While oRG cells proliferated within 1 wpi, the peak of the OPC expansion was observed at 2 wpi (Figures 3A–3C, S3A, and S3B). Consistent with our observations

Figure 2. oRGs increase their proliferative capacity after ischemic brain injury in piglets
(A) Experimental scheme.
(B) Photographic image of the coronal plane of piglet brain tissue including anterior SVZ at 2 weeks of age. Arrow indicates the injection site of endothelin-1.
(C) Coronal section of piglet brains at 1 wpi, stained for MBP (magenta). Dashed lines indicate the borders between the ISVZ and OSVZ and between the OSVZ and PVWM. These are composite images of six separate fields (three vertical and two horizontal tiles).
(D) Percent MBP coverage ($n = 4$, biological replicates).
(E) Coronal section of piglet PVWM at 1 wpi, stained for Iba1 (green) at low magnification (top) and high magnification (bottom).
(F) Coronal section of piglet PVWM in control or injury groups at 1 (top) and 4 wpi (bottom), stained for CC1 (red).
(G) Density of CC1$^+$ cells in piglet PVWM (1 wpi: $n = 3$, 2 wpi: control $n = 3$, injury $n = 5$, 4 wpi: $n = 4$, biological replicates).
(H) Coronal section of piglet DL-SVZ in control or injury (1 wpi) groups, stained for DAPI (blue). Dashed lines indicate the borders between the ISVZ and OSVZ and between the OSVZ and PVWM.
(I) Thickness of the DL-SVZ of piglets (control $n = 6$, injury $n = 3$, biological replicates).
(J) Sox2$^+$Hopx$^+$Ki67$^+$ cells in the OSVZ of piglets.
(K and L) Density of Ki67$^+$ cells (control $n = 7$, injury $n = 6$, biological replicates) and (L) Sox2$^+$Hopx$^+$Ki67$^+$ cells ($n = 3$, biological replicates).
(M) Coronal section of the DL-SVZ of piglets in controls stained for Hopx (red) and Ki67 (white). Dashed lines indicate the border between the ISVZ and OSVZ.
(N) Hopx$^+$Ki67$^+$ density in control OSVZ ($n = 3$, biological replicates).
(O) Coronal section of piglet DL-OSVZ in control or injury groups, stained for Hopx (red) and Ki67 (white).
(P–R) Density of Hopx$^+$ (P), Hopx$^+$Ki67$^+$ (Q), and Ki67$^+$ (R) cells in piglet OSVZ ($n = 3$, biological replicates).
Data are represented as mean ± SEM. Statistical analyses: (D, I) unpaired t test; (G, K, L) two-way ANOVA with Sidak's multiple comparisons test; (N, P–R) one-way ANOVA with Tukey's multiple comparisons test. *$p < 0.05$, **$p < 0.01$, ***$p < 0.001$, ****$p < 0.0001$. Scale bar: (C) 200 μm, (E) 50 μm (top) and 20 μm (bottom), (F) 50 μm, (H) 50 μm, (J) 20 μm, (M) 50 μm, and (O) 50 μm. See also Figure S2.

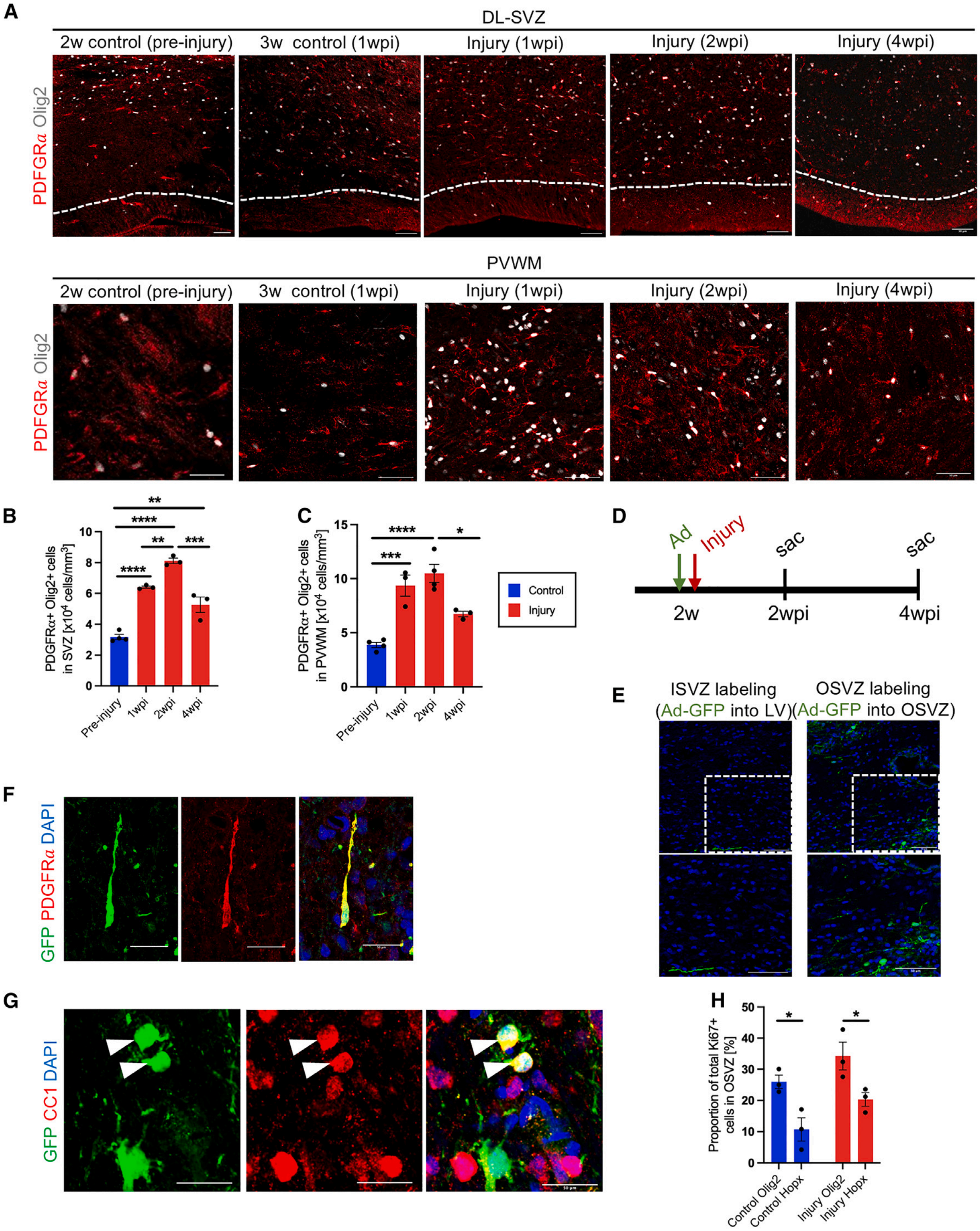

Figure 3. Brain injury enhances the production of OSVZ OPCs, which migrate to the PVWM lesion to generate mature oligodendrocytes

(A) Coronal section of the DL-SVZ (top) and PVWM (bottom) of piglets in control or injury groups, stained for PDGFRα (red) and Olig2 (white).

(B and C) Density of PDGFRα$^+$Olig2$^+$ cells in piglet DL-SVZ (B) and PVWM (C) (*n* = 3–4, biological replicates).

(D) Experimental scheme.

(E) Coronal section of piglet PVWM at 2 wpi, stained for GFP (green) and DAPI (blue).

(F) Representative image of GFP$^+$ (green) OSVZ-derived PDGFRα$^+$ (red) OPCs at 2 wpi within PVWM, stained for DAPI (blue).

(legend continued on next page)

in the human SVZ, most OPCs in the piglet SVZ were located in the OSVZ, but not in the ISVZ (Figure 3A), and increased their number after injury (Figure S3C). To assess the origin of OPCs, we labeled ISVZ or OSVZ cells by injecting GFP-encoding adenovirus into the lateral ventricle or OSVZ, respectively, before injecting endothelin-1 (Figures 3D and S3D). The majority of labeled cells in the ISVZ were Sox2$^+$ NSCs (96.3% ± 1.3%) (Figures S3E–S3G and S3L). In the OSVZ, approximately 45% of GFP$^+$ level cells were NSCs (Sox2, 44.9% ± 5.4%) (Figures S3H and S3M). In addition to Dcx$^+$ neuroblasts, a significant amount of labeled OSVZ cells were Hopx$^+$ oRG (32.0% ± 6.7%) and Olig2$^+$ oligodendrocyte lineage cells (26.5% ± 4.8%) (Figures S3I–S3K and S3M). While there were no GFP$^+$ ISVZ-derived cells in the PVWM at 2 wpi, we observed GFP$^+$ cells derived from the OSVZ in the injured PVWM (Figure 3E). Notably, several OSVZ-derived GFP$^+$ cells in the PVWM expressed platelet derived growth factor receptor alpha (PDGFRα) (Figure 3F), indicating that cells derived from the OSVZ contribute to the expansion of OPCs in the injured PVWM. Furthermore, we observed OSVZ-derived mature oligodendrocytes located in the PVWM region at 4 wpi (Figure 3G), suggesting that the ischemic injury results in the production of OSVZ OPCs that migrate toward the lesion and differentiate into mature oligodendrocytes. Altogether, these findings indicate that neonatal brain injury causes an increase in both oRG cells and OPCs in the OSVZ. While OSVZ OPCs were more proliferative, oRG accounted for approximately 20% of proliferating cells (Figure 3H). During the fetal period, oRG cells are characterized as an important additional source of OPCs for white matter expansion and myelination in the gyrencephalic human and primate brains.[5,37] Therefore, our results suggest postnatal oRG cells as possible important contributors to expansion of the endogenous OPC pool in the OSVZ and regenerative capacity in the neonatal brain after injury.

Neonatal ischemic injury downregulates pro-oligodendrocyte transcription factors in both oRG and vRG cells

As our findings suggest that oRG cells may play an important role in OPC expansion after ischemic white matter injury, we next assessed injury-induced changes in the molecular profiles of oRG in the OSVZ and compared these profiles with those of NSCs in the ISVZ (hereinafter called ventricular radial glia [vRG]). Based on the timing of peak OSVZ proliferation post injury, oRG and vRG cells were isolated by fluorescence-activated cell sorting from the piglet SVZ at 1 wpi. Most of the postnatal piglet Hopx$^+$ oRG cells expressed both glutamate aspartate transporter (GLAST) and CD133 (93.6% ± 1.9% of GLAST$^+$CD133$^+$ OSVZ cells expressed Hopx; 87.8% ± 2.2% of Hopx$^+$ cells expressed both GLAST and CD133) (Figure S4A).[38] Previous studies have shown that vRG and oRG cells in the developing human brain can be distinguished based on CD133 expression levels.[38,39] Consistent with these findings in humans, differential CD133 expression was also observed between the two radial glia populations in the postnatal piglet SVZ (Figures S4B and S4C). Different CD133 expression levels were used to distinguish between GLAST$^+$/CD133^{high} vRG and GLAST$^+$/CD133^{low} oRG within the GLAST$^+$ SVZ cell population (Figure S4D).[40] We also confirmed that isolated vRG and oRG cells displayed the reliable markers of Hopx and CD133 (PROM1) to distinguish between cell types (Figures S4E and S4F).

Our RNA-seq analysis comparing control and injury groups identified a total of 549 differentially expressed genes (DEGs) in isolated oRG cells using a threshold of an adjusted p value < 0.1 with 1.4 of minimal fold change. While 319 DEGs were shared in both oRG and vRG cells (231 upregulated, 87 downregulated, and 1 upregulated in oRG but downregulated in vRG), 230 DEGs (222 upregulated, 8 downregulated) and 975 DEGs (69 upregulated, 906 downregulated) were specifically identified in oRG and vRG cells, respectively (Figures 4A–4C). When we analyzed the 319 DEGs observed in both oRG and vRG cells, our pathway analysis using Enrichr[41–43] predicted signaling pathways associated with microglia, oligodendrocyte specification, and immune responses (Figure 4D). Genes involved in oligodendrocyte specification (*Olig1*, *Olig2*, *Nkx2.2*, *Sox8*, and *Cnp*) were downregulated in both oRG and vRG cells after brain injury (Figures 4E and 4F). These genes have been previously implicated in the differentiation of NSCs to oligodendrocyte lineage cells.[19,44–46] Finally, to validate the RNA-seq results, we performed immunohistochemical analyses for Olig1, Olig2, and Nkx2.2 in control and injured piglets. The proportions of both oRG and vRG cells expressing Olig1, Olig2, and Nkx2.2 were significantly decreased at 1 wpi (Figures 4G–4J and S4G–S4J). These results indicate that neonatal ischemic injury downregulates the expressions of pro-oligodendrocyte transcription factors in both oRG and vRG cells.

The ATF5 pathway is upregulated in oRG cells after brain injury to regulate cell proliferation and apoptosis

To identify oRG-specific molecular changes after ischemic injury, we assessed 230 DEGs identified only within oRG cells. Pathway analysis of these DEGs predicted signaling pathways associated with vascular endothelial growth factor (VEGF), microglia, and apoptosis modulation (Figure 5A). Several genes involved in apoptosis modulation, including *Atf5*, *Mcl1*, *Bag3*, and *Bcl2a1*, were upregulated in oRG (Figures 5B and 5C). ATF5 acts as an anti-apoptotic transcription factor[47] and is expressed in NSCs of the rodent ventricular zone and SVZ to maintain progenitor cell proliferation and inhibit their differentiation.[48–50] Myeloid cell leukemia sequence 1 (MCL1), a downstream effector of ATF5, is also expressed in postnatal SVZ NSCs and regulates cell survival to sustain neurogenesis.[51,52] MCL1 modulates cell proliferation through multiple interactions with cell cycle regulators.[53] Bcl2-associated athanogene 3

(G) Representative image of GFP$^+$ (green) OSVZ-derived CC1$^+$ (red) oligodendrocytes within PVWM, stained for DAPI (blue).

(H) Proportions of Olig2$^+$ or Hopx$^+$ cells in OSVZ Ki67$^+$ cells (n = 3, biological replicates).

Data are represented as mean ± SEM. Statistical analyses: (B, C) one-way ANOVA with Tukey's multiple comparisons test; (H) unpaired t test. *$p < 0.05$, **$p < 0.01$, ***$p < 0.001$, ****$p < 0.0001$. Scale bar: (A) 50 μm, (E) 50 μm, (F) 50 μm, and (G) 50 μm. See also Figure S3.

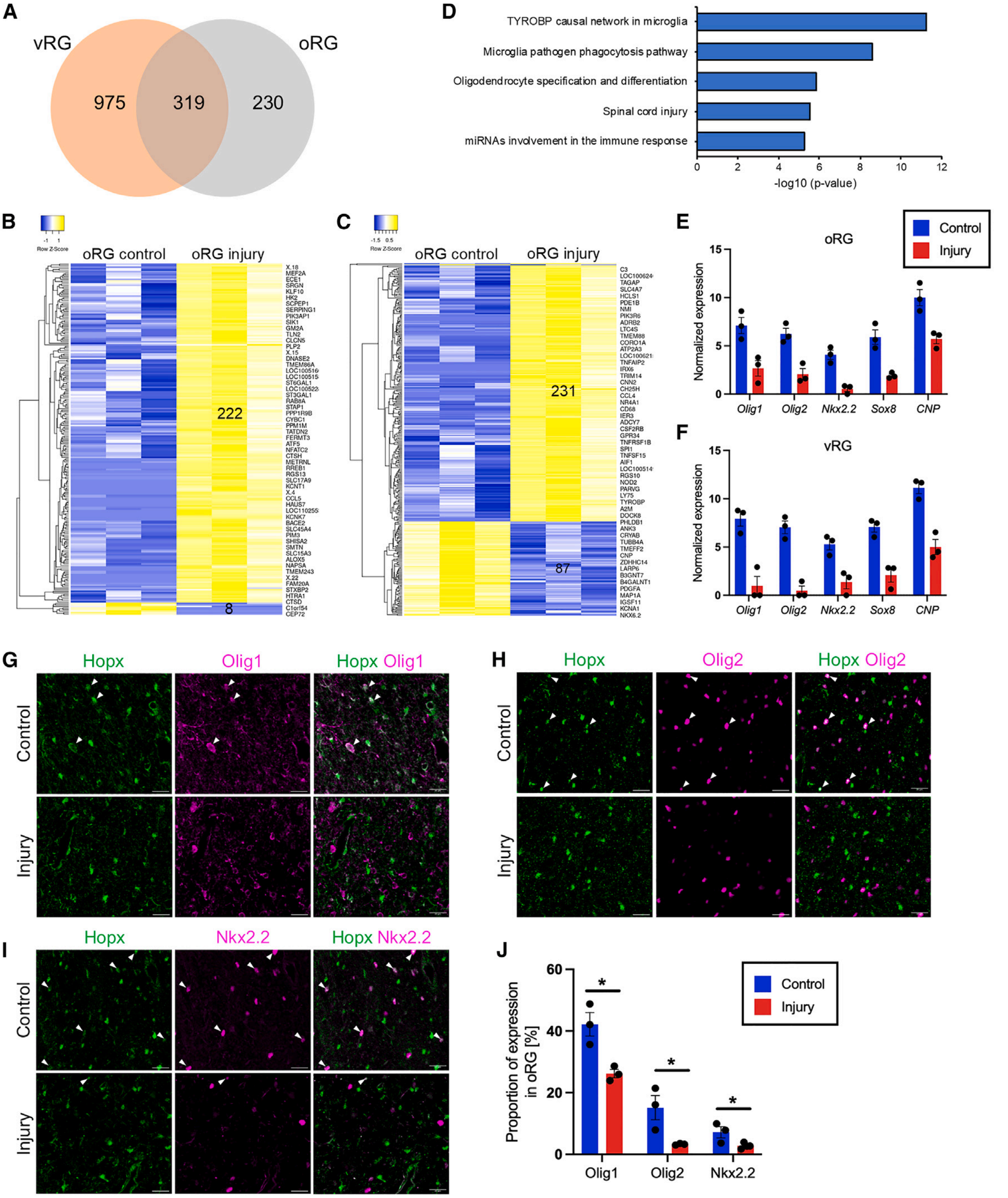

Figure 4. Neonatal ischemic injury downregulates pro-oligodendrocyte transcription factors in both oRG and vRG cells

(A) Venn diagram displaying the number of shared and distinct DEGs identified from oRG and vRG RNA-seq datasets.

(B) Heatmap of the 230 DEGs specific to the oRG dataset.

(C) Heatmap of the 318 DEGs shared by oRG and vRG RNA-seq datasets.

(D) Predicted pathways from Enrichr analysis of DEGs shared by oRG and vRG (determined by directional *Z* scores) in injury compared to control.

(E and F) Normalized expression of oligodendrocyte specification genes that were altered by brain injury in oRG (E) and vRG (F).

(G–I) Coronal section of piglet OSVZ in control or injury (1 wpi), stained for Hopx (green) with Olig1 (G), Olig2 (H), or Nkx2.2 (I) (magenta). Arrowheads indicate the presence of Olig1, Olig2, or Nkx2.2 expression in oRG.

(J) The percentage of Hopx^+ oRG expressing Olig1, Olig2, or Nkx2.2 in piglet OSVZ ($n = 3$–4, biological replicates).

Data are represented as mean ± SEM. Statistical analysis: (J) unpaired t test. $^*p < 0.05$. Scale bar: (G–I) 20 μm. See also Figure S4.

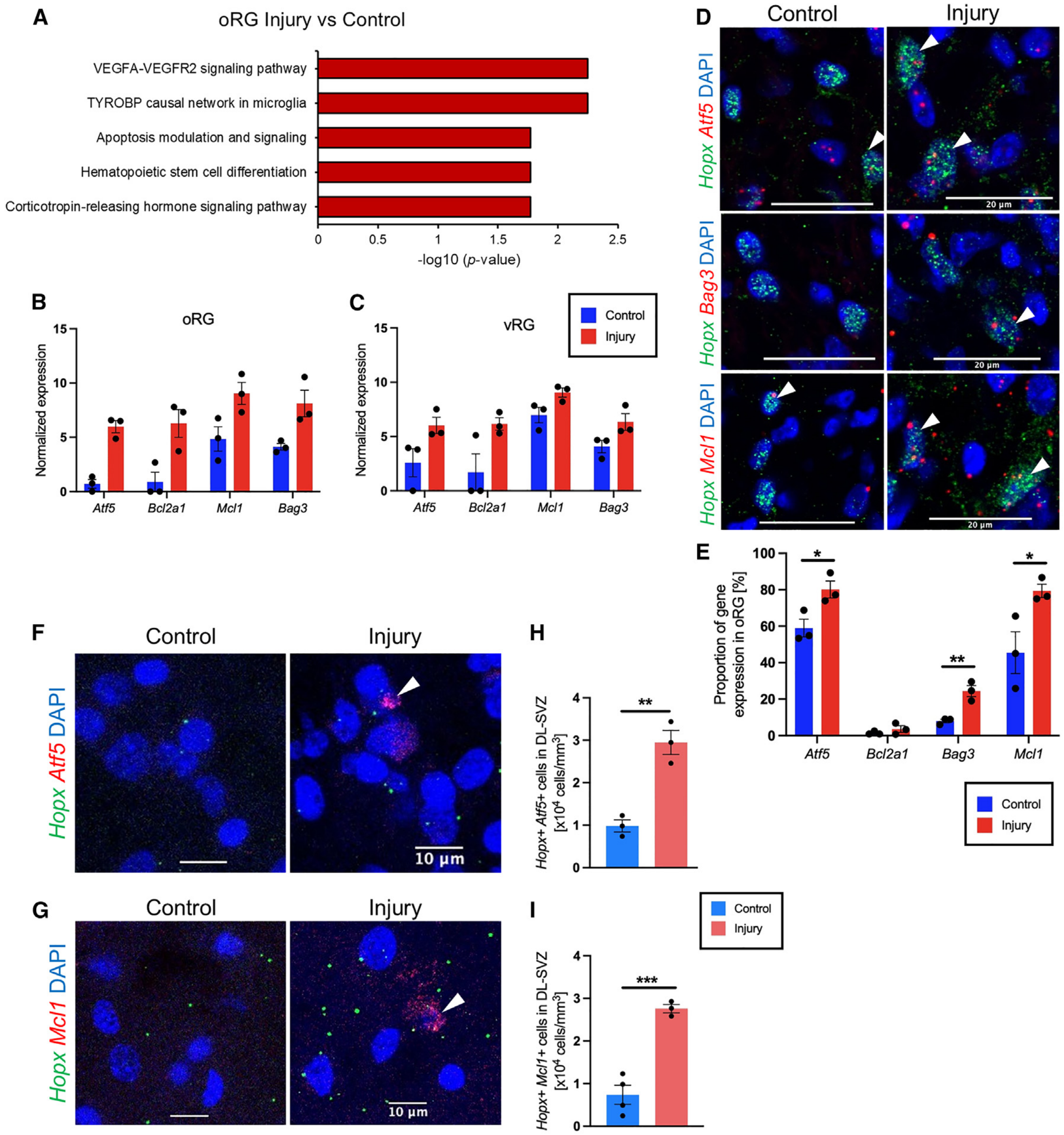

Figure 5. ATF5 pathway genes are specifically upregulated in oRG cells after brain injury

(A) Predicted pathways from Enrichr analysis of DEGs specific to oRG (determined by directional *Z* scores) in injury compared to control.

(B and C) Normalized expressions of apoptosis modulation genes that were altered by brain injury in oRG (B) and vRG (C).

(D) Coronal section of piglet OSVZ in control or injury (1 wpi) groups. Arrowheads indicate the presence of *Atf5*, *Bag3*, or *Mcl1* mRNA puncta within the Hopx$^+$ oRG cells.

(E) The percentage of Hopx$^+$ oRGs that contain *Atf5*, *Bcl2a1*, *Bag3*, or *Mcl1* mRNA puncta in piglet OSVZ ($n = 3$, biological replicates).

(F and G) RNAscope labeling of coronal sections of human infant DL-OSVZ in control or ischemic injury groups, with the presence of mRNA puncta of *Atf5* (F, red) and *Mcl1* (G, red) with *Hopx* (green).

(H and I) The density of cells that contain *Atf5*$^+$*Hopx*$^+$ (H) or *Mcl1*$^+$*Hopx*$^+$ (I) mRNA puncta in the DL-OSVZ ($n = 3$–4, biological replicates).

Data are represented as mean ± SEM. Statistical analyses: (E, H, and I) unpaired t test. *$p < 0.05$, **$p < 0.01$, ***$p < 0.001$. Scale bar: (D) 20 μm, (F) 10 μm, and (G) 10 μm. See also Figure S5.

(BAG3) is known to stabilize MCL1 expression, promoting anti-apoptotic activity of cancer cells.[54,55] Previous studies have indicated that BAG3 plays a key role in regulating the proliferation rate of neural progenitor cells.[56]

These findings led to our hypothesis that upregulation of these genes in oRG cells promotes their proliferation as a response to ischemic injury. When the expression of *Atf5*, *Mcl1*, *Bag3*, and *Bcl2a1* was assessed *in vivo*, we observed a significant increase

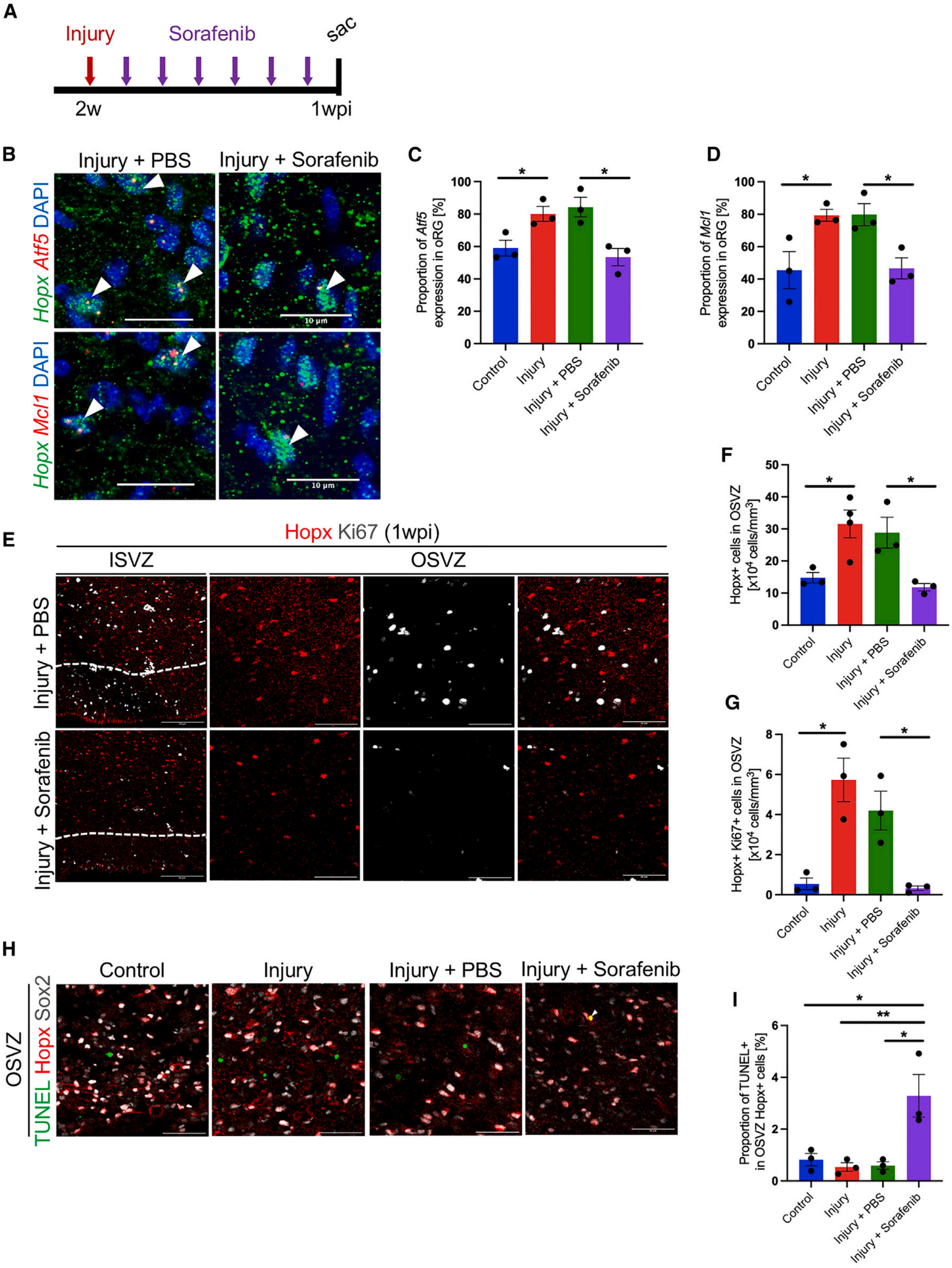

Figure 6. ATF5 pathway regulates oRG proliferation and apoptosis

(A) Experimental scheme.

(B) Coronal section of piglet OSVZ in injury (1 wpi) with PBS treatment and sorafenib treatment groups. Arrowheads indicate the presence of *Atf5* or *Mcl1* mRNA puncta within the Hopx^{+} oRG.

(legend continued on next page)

in *Atf5*, *Mcl1*, and *Bag3* expression in piglet oRG cells after injury (Figures 5D and 5E). In contrast, no change in the expression of these genes was observed in vRG cells (Figures S5A and S5B). Importantly, we also confirmed that the expression of *Atf5* and *Mcl1* was increased in oRG cells after human infant brain injury (Figures 5F–5I). These results indicate that ATF5 pathway genes are selectively upregulated in human and piglet postnatal oRG cells—but not in vRG cells—in response to neonatal brain injury.

Sorafenib, an RAF kinase inhibitor, decreases the levels of ATF5 and MCL1 by inhibiting CREB3L2 and ATF5 binding to *Atf5* and *Mcl1* promoters, respectively.[51] To determine whether the ATF5 pathway is functionally involved in injury-induced proliferation of postnatal oRG cells, sorafenib was intranasally administered to piglets for 6 days after brain injury (Figure 6A). This treatment significantly inhibited the injury-induced increase in *Atf5* and *Mcl1* expressions in oRG cells (Figures 6B–6D). Furthermore, sorafenib decreased the density of both proliferating oRG and total oRG cells after injury (Figures 6E–6G) and did not affect the density of OPCs at this time point (Figure S5C), pointing to a specific role of the ATF5 pathway in injury-induced oRG cell proliferation.

When we analyzed cell apoptosis in the piglet brain using TdT-mediated dUTP-biotin nick-end labeling (TUNEL), TUNEL$^+$ apoptotic cells were observed in the injured PVWM at 1 wpi (Figure S5D). The density of apoptotic cells in the whole SVZ region was significantly increased after brain injury (Figures S5D and S5E). Importantly, we found an upregulation of the ATF5 pathway specifically in oRG cells after white matter injury in humans and piglets (Figures 5D and 5E). Consistent with the previously established role for the ATF5 pathway in suppressing apoptosis, injury-induced apoptosis was not observed in oRG cells (Figures 6H and 6I). Conversely, sorafenib-induced inhibition of the ATF5 pathway caused apoptosis in both NSCs and oRG cells within the OSVZ (Figures 6H, 6I, S5E, and S5F), indicating that activation of the endogenous ATF5 pathway constitutively protects oRG cells from cell apoptosis induced by ischemic white matter injury. Altogether, our data demonstrate a critical role for ATF5 activation in the proliferation and survival of oRG cells after neonatal brain injury.

Intranasal ATF5 activation promotes OSVZ-derived oligodendrogenesis in the injured PVWM

Salubrinal is an inhibitor of eukaryotic initiation factor 2 subunit α (eIF2α) dephosphorylation and increases ATF5 levels through eIF2α phosphorylation.[57,58] To further assess the role of the ATF5 pathway in oRG proliferation, salubrinal was administered intranasally to piglets maintained under normal physiological conditions (no neonatal brain injury) for 7 days (Figure S6A). In the uninjured piglet brain, intranasal salubrinal treatment significantly increased both *Atf5* and *Mcl1* expression in oRG cells to levels similar to those observed after neonatal brain injury (Figures S6B–S6D). Furthermore, intranasal ATF5 activation alone increased the numbers of both proliferating and total oRG cells in the OSVZ. The expansion and proliferation of oRG cells induced by ATF5 activation were similar in magnitude to those observed after neonatal ischemic injury (Figures S6E–S6G), suggesting that ATF5 activation maintains oRG cell proliferation both under normal physiological conditions and after neonatal injury. This conclusion was also supported by the temporal change observed in post-injury oRG cell proliferation (Figure 2O), which was consistent with the significant increase in *Atf5* and *Mcl1* expression found in oRG cells at 1 wpi that returned to pre-injury levels at 2 wpi (Figures S6H–S6J). Involvement of ATF5 signaling was further confirmed by observing an increase in eIF2α phosphorylation without changes in total eIF2α (Figures S6K–S6N). When we assessed total and proliferating OPCs after 7 days of salubrinal treatment, there were no significant differences in the numbers (Figures S6O–S6Q), indicating limited direct effects of ATF5 activation on endogenous OPC proliferation.

Our results indicate a significant contribution of postnatal oRG cells to OPC production. On the other hand, the increase of *Atf5* expression in oRG is limited within 1 week after injury (Figures S6H–S6J). We therefore tested whether the extension of ATF5 activation enhances OSVZ-derived oligodendrogenesis following neonatal ischemia. Salubrinal was given to the piglet intranasally for 7 consecutive days from day 8 to day 14 post injury, and brains were analyzed at 4 wpi (Figure 7A). Neonatal brain injury without salubrinal treatment caused a reduction in the density of CC1$^+$ mature oligodendrocytes in the PVWM, as compared to uninjured controls (Figures 7B and 7C). Notably, extended ATF5 activation with intranasal salubrinal treatment significantly attenuated the ischemia-induced decline of mature oligodendrocytes at 4 wpi (Figures 7B and 7C). Consistent with this finding, intranasal ATF5 activation improved the injury-induced reduction in MBP expression detected in the PVWM at 4 wpi (Figures 7B–7D). On the other hand, these improvements were not induced by PBS treatment. Furthermore, *in vivo* cell labeling of OSVZ cells demonstrated that the extension of ATF5 activation significantly increased the number of GFP$^+$CC1$^+$ OSVZ-derived oligodendrocytes within the injured PVWM at 4 wpi (Figures 7E and 7F). Most of the OSVZ-derived mature oligodendrocytes were observed in the deep PVWM area (Figure S7A). Salubrinal treatment significantly increased the percentage of GFP$^+$ in total CC1$^+$ cells (Figure S7B). These results indicate that extended ATF5 activation promotes OSVZ-derived

(C and D) The percentage of Hopx$^+$ oRGs that contain *Atf5* (C) or *Mcl1* (D) ($n = 3$, biological replicates) mRNA puncta in piglet OSVZ. Data of control and injury groups are from Figure 5E.

(E) Coronal section of the DL-ISVZ and OSVZ of piglets in injury (1 wpi) with PBS treatment and sorafenib treatment groups, stained for Hopx (red) and Ki67 (white). Dashed lines indicate the border between the ISVZ and OSVZ.

(F and G) Density of Hopx$^+$ (F) or Hopx$^+$Ki67$^+$ (G) cells in piglet OSVZ ($n = 3$–4, biological replicates). Data of injury groups are from Figures 2P and 2Q.

(H) Coronal section of the piglet OSVZ in control, injury, injury with PBS treatment, and injury with sorafenib treatment groups, stained for TUNEL (green), Hopx (red), and Sox2 (white).

(I) The percentage of Hopx$^+$ cells expressing TUNEL in the OSVZ ($n = 3$, biological replicates).

Data are represented as mean ± SEM. Statistical analyses: (C, D, F, and G) unpaired t test; (I) one-way ANOVA with Tukey's multiple comparisons test. $^*p < 0.05$, $^{**}p < 0.01$. Scale bar: (B) 10 μm, (E) 20 μm, and (H) 20 μm. See also Figure S5.

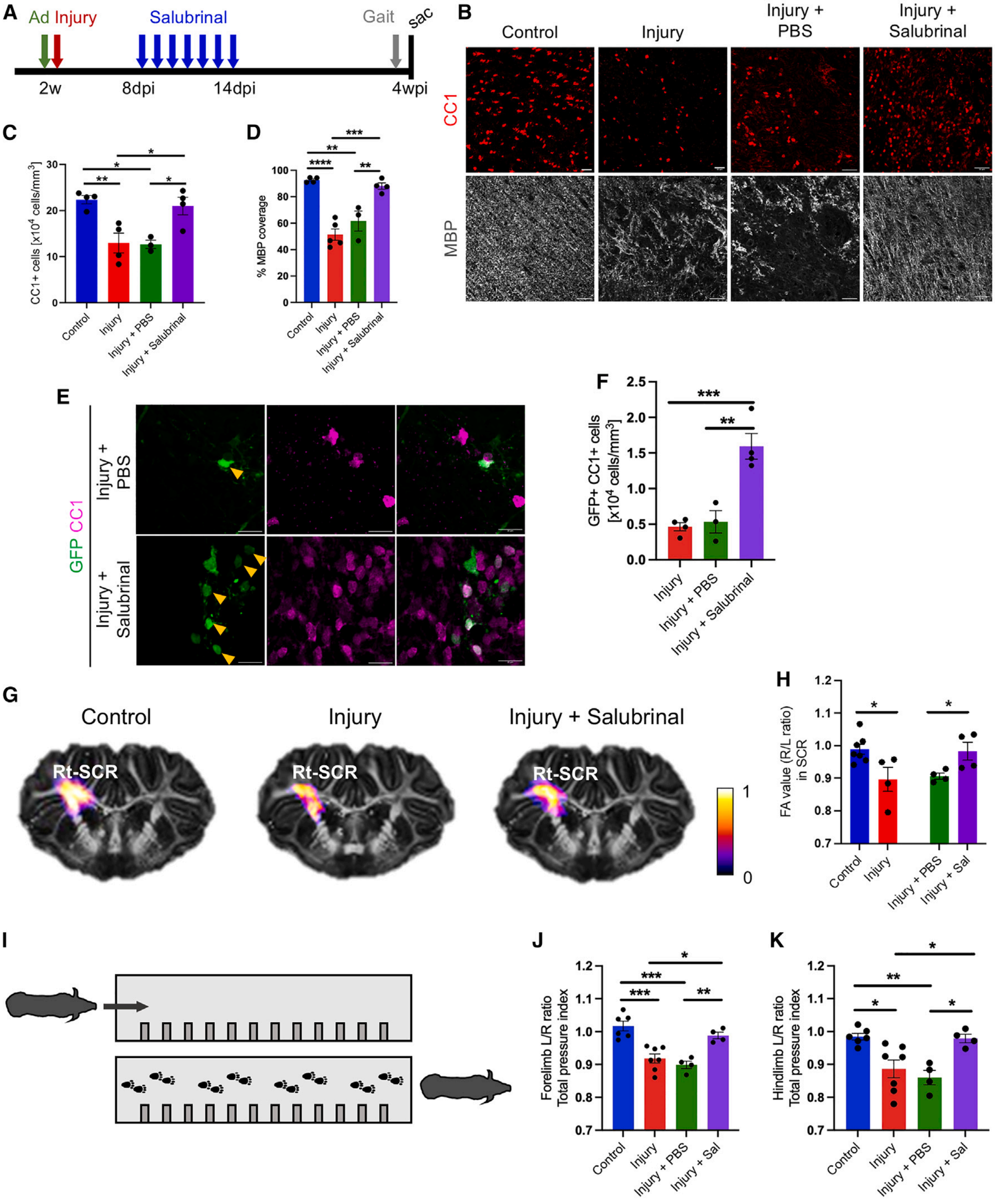

Figure 7. Intranasal ATF5 activation promotes OSVZ-derived oligodendrogenesis in the injured PVWM and improves impairment of gait behaviors

(A) Experimental scheme.

(B) Coronal section of the PVWM of 6-week (4 wpi) piglets in control, injury, injury with PBS treatment, or injury with salubrinal treatment groups, stained for CC1 (upper, red) or MBP (bottom, white). Images of CC1 staining in control and injury groups are from Figure 2F.

(C) Density of CC1$^+$ cells in piglet PVWM. Data of control and injury groups are from Figure 2G (*n* = 3–4, biological replicates).

(D) Percent coverage by MBP (*n* = 3–5, biological replicates).

(E) Representative images of GFP$^+$ (green) OSVZ-derived CC1$^+$ (magenta) oligodendrocytes within PVWM at 4 wpi in PBS treatment or salubrinal treatment groups.

(F) Density of GFP$^+$CC1$^+$ cells in piglet PVWM (*n* = 3–4, biological replicates).

(legend continued on next page)

oligodendrogenesis after ischemic white matter injury. When we investigated the potential pro-differentiative effect of salubrinal on OPCs using a primary glial cell culture, salubrinal treatment did not enhance oligodendrocyte differentiation (Figures S7C–S7L), suggesting that intranasal salubrinal treatment acts on oRG rather than OPCs to promote oligodendrogenesis.

Intranasal ATF5 activation improves microstructural alterations and gait behavior impairments induced by neonatal white matter injury

To assess microstructural maturation of the developing white matter of the piglet after neonatal ischemia, high-resolution DTI was performed at 4 wpi. Consistent with previous results obtained in human PVWM injury,[59,60] we observed a significant reduction in FA in the superior corona radiata corresponding to the dorsal PVWM region—shown as a decrease in right-left ratio. Importantly, the FA reduction caused by ischemia was significantly attenuated by salubrinal treatment (Figures 7G and 7H; Table S2), suggesting that intranasal ATF5 activation also improved the white matter microstructural alterations induced by ischemic injury.

Ischemic PVWM damage in the human neonate is significantly associated with motor deficits such as spasticity and unsteady gait behavior.[27,61] Therefore, as an index of functional/behavioral outcome, we analyzed spontaneous gait behavior in piglets after brain ischemia by performing GaitFour analysis (Figure 7I and Video S1).[62] This system allows us to analyze a variety of aspects related to gait behavior, including spatial, temporal, and pressure parameters (Figures 7J, 7K, and S7M–S7T). Ischemic PVWM injury caused a decrease in weight distribution toward the injury-affected limbs, as determined by lower left-right ratio of pressure values in both forelimbs and hindlimbs. Notably, intranasal ATF5 activation significantly improved this gait disturbance caused by ischemic injury (Figures 7J, 7K, S7S, and S7T).

Collectively, our results indicate that non-invasive intranasal ATF5 activation in the piglet brain after neonatal ischemia not only crucially promotes OSVZ-derived oligodendrogenesis in the PVWM but also improves microstructural and behavioral impairment caused by ischemia-induced white matter injury.

DISCUSSION

This study is the first to reveal increased oRG proliferation and enhanced OPC production after ischemic injury in both human infants and a neonatal porcine model. Our *in vivo* cell labeling method shows that OSVZ-derived OPCs migrate toward injured white matter and differentiate into mature oligodendrocytes. While neonatal ischemia downregulates pro-oligodendrocyte transcription factors in both oRG and vRG cells, results from our RNA-seq demonstrates a critical role for ATF5 activation in the proliferation and survival of oRG cells after injury. Notably, intranasal ATF5 activation after neonatal ischemia promotes OSVZ-derived oligodendrogenesis and remyelination of the injured white matter. Furthermore, our studies identify that this pharmacological intervention limits microstructural alterations in white matter and improves the impairment of motor functions resulting from ischemic white matter injury. These findings reveal a novel role for oRG cells and the OSVZ in the early postnatal period and identify ATF5 as a potential therapeutic target for infants with white matter injury.

Little is known about the response of oRG to perinatal brain injury.[63] This project utilizes both postmortem human tissues and a highly translational piglet model to target and manipulate oRG to understand the role of these cells in recovery from ischemic injury. The piglet brain is a highly evolved gyrencephalic system with a percentage of white matter similar to humans. In addition, the maturation pattern in piglet white matter displays a developmental progression similar to human white matter.[54,55] We have previously shown that the early postnatal piglet SVZ closely resembles its human counterpart,[24] making it an ideal system for studying the contribution of oRG to white matter regeneration.[64] The oRG cell type is unique to humans and other higher-order mammals and contributes to increased cortical complexity.[34] oRG cells have also been shown to produce a glio-genic intermediate, the pre-OPC, demonstrating that oRGs can be an additional source for OPC regeneration.[5,65] Our present study shows that postnatal oRG cells contribute to endogenous regeneration in both human and piglet white matter. In our previous studies in mouse, we have elucidated endogenous regulators of oligodendrocyte regeneration in white matter from SVZ OPCs.[16] We also showed that OPCs migrating from the SVZ receive transient glutamatergic synapses and directly contribute to remyelination after demyelinating injury.[66] Further comparative studies in piglet and human will assist in understanding the complexity of the cellular and physiological events underlying repair and remyelination of the gyrencephalic white matter after neonatal ischemia.

Our sequencing data in piglet, together with our analysis in human tissue, demonstrate increased expression of *Mcl1* and *Atf5* in oRG cells following ischemic injury. Consistent with these findings, *Atf5* has been identified as a stress response gene that is upregulated in response to various insults—including endoplasmic reticulum stress, heat stress, amino acid limitation, and oxidative stress.[67] *Atf5* is a transcription factor within the basic leucine zipper family, which plays a critical role in cell survival and promotes proliferation in NSCs and the central nervous system.[48,49]

(G) Representative FA maps of the superior corona radiata (SCR) region from DTI analysis using piglet brains in control (6 weeks), injury (4 wpi), and injury with salubrinal treatment (4 wpi). Color code indicates the right-left ratio of FA values.

(H) Right-left ratio of FA values in the superior corona radiata of piglet brains (n = 4–7, biological replicates).

(I) Overview of gait behavior tests using GaitFour system. When piglets walk on the GaitFour mat, semi-automated gait pattern analysis was conducted using the GAITFour software.

(J and K) Left-right ratios of total pressure index of forelimbs (J) and hindlimbs (K) in control (6 weeks), injury (4 wpi), injury (4 wpi) with PBS or salubrinal treatment (n = 4–7, biological replicates).

Data are represented as mean ± SEM. Statistical analyses: (C, D, F, J, and K) one-way ANOVA with Tukey's multiple comparisons test; (H) unpaired t test. $^{*}p < 0.05$, $^{**}p < 0.01$, $^{***}p < 0.001$, $^{****}p < 0.0001$. Scale bar: (B) 50 μm and (E) 20 μm. See also Figures S6 and S7, Table S2, and Video S1.

Atf5 expression is modulated by upstream activation of fibroblast growth factor receptor and epidermal growth factor receptor signaling.[51] Interestingly, we previously demonstrated that intranasal administration of heparin-binding epidermal growth factor enhances the generation of new oligodendrocytes and promotes functional recovery after neonatal hypoxic brain injury in mice.[17] Importantly, by using pharmacological manipulation in the piglet brain, our present study shows that inhibitions of injury-induced *Mcl1* and *Atf5* upregulation cause reduced proliferation and increased cell death of Hopx$^+$ oRG cells after ischemia. In addition, ATF5 activation using the eIF2 phosphatase inhibitor (salubrinal) increases oRG proliferation in uninjured animals. Salubrinal is known to support a pro-survival mechanism in neurons.[58] In our study, intranasal modulation of the *Atf5* pathway following injury led to the proliferation and survival of oRG cells and enhanced oligodendrogenesis. However, *Atf5* is not specific to oRG. Although we did not observe significant effects of salubrinal treatment on endogenous OPC proliferation and oligodendrocyte differentiation, we are unable to completely rule out any direct effects on OPCs. Furthermore, salubrinal is not specific to the ATF5 pathway and exhibits neuroprotective effects through additional mechanistic pathways.[26] Introduction of modern genetic techniques in the piglet brain will be required for an in-depth investigation of the contribution of the ATF5 pathway to the maintenance of perinatal oRG cells and enhancement of oligodendrogenesis.

Intranasal administration is an intriguing method for delivering therapeutics to the central nervous system, as it is a non-invasive way to bypass the blood-brain barrier.[68] Previous rodent studies have shown the vast possibilities of using this approach to improve myelination. For example, intranasal treatment with mesenchymal cells, oligonucleotides, and drugs has been shown to enhance myelination in rodent models.[69–71] Thus, intranasal salubrinal treatment is clinically feasible and a possible translational approach in infants with white matter injury.

Microstructural alterations determined by DTI, such as decreased FA, are important biomarkers in human infants after white matter injury.[59,60] Since PVWM includes the pyramidal tract, focal damage in this region leads to spasticity of contralateral limbs causing gait abnormalities.[14,61] Importantly, the clinically relevant structural and behavioral gait impairments identified in humans are replicated in our piglet model of neonatal ischemic white matter injury. Gait analysis is commonly used to quantitatively assess gait abnormalities to provide information about diagnosis, assessment, monitoring of disease progression, and predictions for interventions.[72] Assessment of gait function has been used extensively in patients with cerebral palsy to assess the severity, extent, and nature of physical deficits to aid in treatment decisions.[72] In the present study, we developed and employed a variety of locomotor assessments in our piglet model, allowing us to analyze the efficacy of a potential therapeutic intervention on functional recovery after ischemia. Notably, in addition to cellular and structural recovery, our results show that salubrinal treatment during a critical time window after injury improves ischemia-induced impairment of gait function. Furthermore, consistent with previous *in vitro* and *in vivo* testing in a variety of pre-clinical studies demonstrating that salubrinal has no adverse effects,[73,74] we also found that this stress response modulator had no unfavorable behavioral effects in our piglet injury model.

Currently, there are very few treatment options available for white matter regeneration after ischemic injury in infants. Given that the non-invasive intranasal approach is a clinically feasible route for pharmacological treatment, brief intranasal salubrinal treatment has a significant translational potential to minimize apoptosis and enhance oRG proliferation after neonatal brain injury, with subsequent enhancement of oligodendrogenesis and remyelination. Our study not only highlights the important roles of oRG cells and the OSVZ in response to neonatal ischemia but also indicates that modulating survival and proliferation of oRG cells is a viable therapeutic avenue for cellular, structural, and functional recovery in infants with white matter injury.

Limitations of the study

Although our data support the critical role of oRG cells as regenerative cells for OPC production and white matter repair after injury, there are significant challenges to direct lineage tracing using a transgenic system in piglet models.[75] While the use of GFP-adenovirus allowed us to track OSVZ-derived mature oligodendrocytes following ischemic injury, we were unable to directly observe oRG-derived OPCs. Additionally, OPC isolation and culture in the piglet brain have not been established. As a result, our *in vitro* cell culture experiments were performed using mice rather than piglets. Furthermore, we cannot entirely exclude the possibility that some of the Hopx$^+$ cells might already be fate-restricted glial precursors. A previous study in macaques suggests that, at advanced stages of prenatal development—during a period of rapid cerebrum enlargement and gyrification—the primary role of oRG cells shifts toward glial generation.[37] In our study, approximately 20% of the proliferating cells in the OSVZ were oRG cells. Likewise, the morphological changes observed in postnatal human and piglet oRG cells after injury mirrored the morphology of fetal oRG cells, which are highly proliferative.[34] Therefore, targeting the modulation of oRG cell proliferation and survival to enhance gliogenesis may aid in promoting white matter regeneration after ischemic injury. Given that analyses using salubrinal were conducted solely in piglets, clinical studies will be required to confirm the effectiveness of this therapeutic strategy in humans.

RESOURCE AVAILABILITY

Lead contact

Further information and requests for resources and reagents should be directed to and will be fulfilled by the lead contact, Vittorio Gallo (vittorio.gallo@seattlechildrens.org).

Materials availability

This study did not generate any new reagents.

Data and code availability

- All RNA-seq data have been deposited to the NCBI Sequence Read Archive (NCBI: PRJNA992775). The accession number is also listed in the key resources table. Raw data from Figures 1, 2, 3, 4, 5, 6, 7, and S1–S7, and Table S2 were deposited on Mendeley at https://doi.org/10.17632/wc2ts3r6dd.1. All data reported in this paper will be shared by the lead contact upon request.

- This paper does not report original code.
- Any additional information required to reanalyze the data reported in this paper is available from the lead contact upon request.

ACKNOWLEDGMENTS

Human tissue was obtained from the NIH NeuroBioBank at the University of Maryland under a material transfer agreement with the NIH and from the Histopathology and Tissue Shared Resource at the Georgetown Lombardi Comprehensive Cancer Center under a material transfer agreement with Georgetown University. We would like to thank Dr. Teodora Orendovici of the Genome Sciences Core at Penn State University School of Medicine for generating the ChIP-seq libraries and performing the sequencing. We would also like to thank Dr. Panagiotis Kratimenos (Children's National Hospital) for his help with human tissue analysis. We thank Dr. Tarik Haydar (Children's National Hospital) for critically reading this manuscript, Drs. Kei Kobayashi and Mobolanle A. Ayodeji (Children's National Hospital) for assistance with animal surgery, and Dr. Jingang Li (Children's National Hospital) for his support in data processing of diffusion tensor imaging. We thank all our colleagues of the Children's National Hospital Research Animal Facility for their support with porcine studies. This work was supported by NIH grant R37NS109478 (Javits Award; V.G.), R01HL139712 (N.I.), R01HL146670 (N.I.), and R21NS127051 (N.I.); research grant JSPS KAKENHI 22K15902 (H.J.), 24K11026 (H.J.), 24K22003 (K.S.), 24H02016 (K.S.), 20H05700 (K.S.), and 23K05770 (K.K.); the Japan Agency for Medical Research and Development (AMED) 23gm1210007 (K.S.); JSPS Core-to-Core program "Neurogenesis Research & Innovation Center (NeuRIC)" JPJSCCA20230007 (K.S.); JSPS Grant-in-Aid for Promotion on Co-Creative Urban Development in Nagoya City University 2412145 (K.S.); The Nitto Foundation (H.J.); Takeda Science Foundation (K.S.); and Grant-in-Aid for Outstanding Research Group Support Program in Nagoya City University grant number 2401101. Research reported in this publication was supported by a Neurodevelopmental Disabilities Research Training grant to L.M.R. from the National Institute of Neurological Disorders and Stroke under award number 5T32NS115656-02. Microscopic analysis was carried out at the Children's National Research Institute, Cell and Tissue Microscopy Core, which is supported by the District of Columbia Intellectual and Developmental Disabilities Research Center award (DC-IDDRC; P50HD105328; V.G.) from the National Institute of Child Health and Human Development. MRI studies were performed at the DC-IDDRC Neuroimaging Core, and animal behavioral studies were performed at the DC-IDDRC Neurobehavioral Evaluation Core. FACS was carried out at the Center for Cancer and Immunology Research, Children's National Hospital Flow Cytometry Core. The content is solely the responsibility of the authors and does not necessarily represent the official views of the NIH or DC-IDDRC. The graphical abstract was created with BioRender.com.

AUTHOR CONTRIBUTIONS

H.J., N.I., and V.G. conceptualized and designed the experiments. H.J., L.M.R., J.P., K.K., and K.S. executed collection and analysis of data. H.J. and S.H. performed animal surgery and behavioral assay. V.K.L., A.A., and T.-W.T. collected and analyzed MRI data. S.Y., Y.I., and K.H.-T. helped with RNA-seq data collection, processing, and analysis. H.J., L.M.R., N.I., and V.G. contributed to manuscript writing. V.G. and N.I. supervised the entire project and provided financial support.

DECLARATION OF INTERESTS

The authors declare no competing interests.

STAR★METHODS

Detailed methods are provided in the online version of this paper and include the following:

- KEY RESOURCES TABLE
- EXPERIMENTAL MODEL AND STUDY PARTICIPANT DETAILS
  - ○ Human brain tissue samples
  - ○ Animals
- METHOD DETAILS
  - ○ Preparation for piglet surgery
  - ○ *In vivo* cell labeling
  - ○ Brain injury
  - ○ Tissue harvest
  - ○ Immunohistochemistry
  - ○ RNAscope *in situ* hybridization
  - ○ Cellular analysis
  - ○ Intranasal drug administration
  - ○ SVZ cell sorting and nuclear isolation
  - ○ RNAseq library preparation and sequencing
  - ○ Primary glial cell culture and immunocytochemistry
  - ○ Behavioral tests
  - ○ DTI acquisition and processing
  - ○ Experimental design
- QUANTIFICATION AND STATISTICAL ANALYSIS

SUPPLEMENTAL INFORMATION

Supplemental information can be found online at https://doi.org/10.1016/j.xcrm.2025.101986.

Received: April 17, 2024
Revised: November 27, 2024
Accepted: February 3, 2025
Published: February 28, 2025

REFERENCES

1. Clowry, G., Molnár, Z., and Rakic, P. (2010). Renewed focus on the developing human neocortex. J. Anat. *217*, 276–288. https://doi.org/10.1111/j.1469-7580.2010.01281.x.
2. Molnár, Z., Clowry, G.J., Šestan, N., Alzu'bi, A., Bakken, T., Hevner, R.F., Hüppi, P.S., Kostović, I., Rakic, P., Anton, E.S., et al. (2019). New insights into the development of the human cerebral cortex. J. Anat. *235*, 432–451. https://doi.org/10.1111/joa.13055.
3. Buyanova, I.S., and Arsalidou, M. (2021). Cerebral White Matter Myelination and Relations to Age, Gender, and Cognition: A Selective Review. Front. Hum. Neurosci. *15*, 662031. https://doi.org/10.3389/fnhum.2021.662031.
4. Hansen, D.V., Lui, J.H., Parker, P.R.L., and Kriegstein, A.R. (2010). Neurogenic radial glia in the outer subventricular zone of human neocortex. Nature *464*, 554–561. https://doi.org/10.1038/nature08845.
5. Huang, W., Bhaduri, A., Velmeshev, D., Wang, S., Wang, L., Rottkamp, C.A., Alvarez-Buylla, A., Rowitch, D.H., and Kriegstein, A.R. (2020). Origins and Proliferative States of Human Oligodendrocyte Precursor Cells. Cell *182*, 594–608.e11. https://doi.org/10.1016/j.cell.2020.06.027.
6. Motavaf, M., and Piao, X. (2021). Oligodendrocyte Development and Implication in Perinatal White Matter Injury. Front. Cell. Neurosci. *15*, 764486. https://doi.org/10.3389/fncel.2021.764486.
7. Liu, Y., Bergmann, T., Mori, Y., Peralvo Vidal, J.M., Pihl, M., Vasistha, N.A., Thomsen, P.D., Seemann, S.E., Gorodkin, J., Hyttel, P., et al. (2021). Development of the Entorhinal Cortex Occurs via Parallel Lamination During Neurogenesis. Front. Neuroanat. *15*, 663667. https://doi.org/10.3389/fnana.2021.663667.
8. Namba, T., and Huttner, W.B. (2017). Neural progenitor cells and their role in the development and evolutionary expansion of the neocortex. Wiley Interdiscip. Rev. Dev. Biol. *6*, e256. https://doi.org/10.1002/wdev.256.
9. Kurinczuk, J.J., White-Koning, M., and Badawi, N. (2010). Epidemiology of neonatal encephalopathy and hypoxic-ischaemic encephalopathy. Early Hum. Dev. *86*, 329–338. https://doi.org/10.1016/j.earlhumdev.2010.05.010.
10. Millar, L.J., Shi, L., Hoerder-Suabedissen, A., and Molnár, Z. (2017). Neonatal Hypoxia Ischaemia: Mechanisms, Models, and Therapeutic

Challenges. Front. Cell. Neurosci. *11*, 78. https://doi.org/10.3389/fncel.2017.00078.

11. Riddle, A., Luo, N.L., Manese, M., Beardsley, D.J., Green, L., Rorvik, D.A., Kelly, K.A., Barlow, C.H., Kelly, J.J., Hohimer, A.R., and Back, S.A. (2006). Spatial heterogeneity in oligodendrocyte lineage maturation and not cerebral blood flow predicts fetal ovine periventricular white matter injury. J. Neurosci. *26*, 3045–3055. https://doi.org/10.1523/jneurosci.5200-05.2006.
12. Back, S.A. (2014). Cerebral white and gray matter injury in newborns: new insights into pathophysiology and management. Clin. Perinatol. *41*, 1–24. https://doi.org/10.1016/j.clp.2013.11.001.
13. Kinney, H.C., and Back, S.A. (1998). Human oligodendroglial development: relationship to periventricular leukomalacia. Semin. Pediatr. Neurol. *5*, 180–189. https://doi.org/10.1016/s1071-9091(98)80033-8.
14. Volpe, J.J. (2001). Neurobiology of periventricular leukomalacia in the premature infant. Pediatr. Res. *50*, 553–562. https://doi.org/10.1203/00006450-200111000-00003.
15. Menn, B., Garcia-Verdugo, J.M., Yaschine, C., Gonzalez-Perez, O., Rowitch, D., and Alvarez-Buylla, A. (2006). Origin of oligodendrocytes in the subventricular zone of the adult brain. J. Neurosci. *26*, 7907–7918. https://doi.org/10.1523/jneurosci.1299-06.2006.
16. Aguirre, A., Dupree, J.L., Mangin, J.M., and Gallo, V. (2007). A functional role for EGFR signaling in myelination and remyelination. Nat. Neurosci. *10*, 990–1002. https://doi.org/10.1038/nn1938.
17. Scafidi, J., Hammond, T.R., Scafidi, S., Ritter, J., Jablonska, B., Roncal, M., Szigeti-Buck, K., Coman, D., Huang, Y., McCarter, R.J., Jr., et al. (2014). Intranasal epidermal growth factor treatment rescues neonatal brain injury. Nature *506*, 230–234. https://doi.org/10.1038/nature12880.
18. Sanai, N., Tramontin, A.D., Quiñones-Hinojosa, A., Barbaro, N.M., Gupta, N., Kunwar, S., Lawton, M.T., McDermott, M.W., Parsa, A.T., Manuel-García Verdugo, J., et al. (2004). Unique astrocyte ribbon in adult human brain contains neural stem cells but lacks chain migration. Nature *427*, 740–744. https://doi.org/10.1038/nature02301.
19. Jakovcevski, I., Filipovic, R., Mo, Z., Rakic, S., and Zecevic, N. (2009). Oligodendrocyte development and the onset of myelination in the human fetal brain. Front. Neuroanat. *3*, 5. https://doi.org/10.3389/neuro.05.005.2009.
20. Sanai, N., Nguyen, T., Ihrie, R.A., Mirzadeh, Z., Tsai, H.H., Wong, M., Gupta, N., Berger, M.S., Huang, E., Garcia-Verdugo, J.M., et al. (2011). Corridors of migrating neurons in the human brain and their decline during infancy. Nature *478*, 382–386. https://doi.org/10.1038/nature10487.
21. Lind, N.M., Moustgaard, A., Jelsing, J., Vajta, G., Cumming, P., and Hansen, A.K. (2007). The use of pigs in neuroscience: modeling brain disorders. Neurosci. Biobehav. Rev. *31*, 728–751. https://doi.org/10.1016/j.neubiorev.2007.02.003.
22. Conrad, M.S., Dilger, R.N., and Johnson, R.W. (2012). Brain growth of the domestic pig (Sus scrofa) from 2 to 24 weeks of age: a longitudinal MRI study. Dev. Neurosci. *34*, 291–298. https://doi.org/10.1159/000339311.
23. Ishibashi, N., Scafidi, J., Murata, A., Korotcova, L., Zurakowski, D., Gallo, V., and Jonas, R.A. (2012). White matter protection in congenital heart surgery. Circulation *125*, 859–871. https://doi.org/10.1161/circulationaha.111.048215.
24. Morton, P.D., Korotcova, L., Lewis, B.K., Bhuvanendran, S., Ramachandra, S.D., Zurakowski, D., Zhang, J., Mori, S., Frank, J.A., Jonas, R.A., et al. (2017). Abnormal neurogenesis and cortical growth in congenital heart disease. Sci. Transl. Med. *9*, eaah7029. https://doi.org/10.1126/scitranslmed.aah7029.
25. Stinnett, G.R., Lin, S., Korotcov, A.V., Korotcova, L., Morton, P.D., Ramachandra, S.D., Pham, A., Kumar, S., Agematsu, K., Zurakowski, D., et al. (2017). Microstructural Alterations and Oligodendrocyte Dysmaturation in White Matter After Cardiopulmonary Bypass in a Juvenile Porcine Model. J. Am. Heart Assoc. *6*, e005997. https://doi.org/10.1161/jaha.117.005997.
26. Matsuoka, M., and Komoike, Y. (2015). Experimental Evidence Shows Salubrinal, an eIF2α Dephosphorylation Inhibitor, Reduces Xenotoxicant-Induced Cellular Damage. Int. J. Mol. Sci. *16*, 16275–16287. https://doi.org/10.3390/ijms160716275.
27. Volpe, J.J. (1981). Neurology of the newborn. Major Probl. Clin. Pediatr. 22, 1–648.
28. Back, S.A. (2017). White matter injury in the preterm infant: pathology and mechanisms. Acta Neuropathol. *134*, 331–349. https://doi.org/10.1007/s00401-017-1718-6.
29. Tsao, C.W., Aday, A.W., Almarzooq, Z.I., Alonso, A., Beaton, A.Z., Bittencourt, M.S., Boehme, A.K., Buxton, A.E., Carson, A.P., Commodore-Mensah, Y., et al. (2022). Heart Disease and Stroke Statistics-2022 Update: A Report From the American Heart Association. Circulation *145*, e153–e639. https://doi.org/10.1161/cir.0000000000001052.
30. Haynes, R.L., Folkerth, R.D., Keefe, R.J., Sung, I., Swzeda, L.I., Rosenberg, P.A., Volpe, J.J., and Kinney, H.C. (2003). Nitrosative and oxidative injury to premyelinating oligodendrocytes in periventricular leukomalacia. J. Neuropathol. Exp. Neurol. *62*, 441–450. https://doi.org/10.1093/jnen/62.5.441.
31. Quiñones-Hinojosa, A., Sanai, N., Soriano-Navarro, M., Gonzalez-Perez, O., Mirzadeh, Z., Gil-Perotin, S., Romero-Rodriguez, R., Berger, M.S., Garcia-Verdugo, J.M., and Alvarez-Buylla, A. (2006). Cellular composition and cytoarchitecture of the adult human subventricular zone: a niche of neural stem cells. J. Comp. Neurol. *494*, 415–434. https://doi.org/10.1002/cne.20798.
32. Brazel, C.Y., Romanko, M.J., Rothstein, R.P., and Levison, S.W. (2003). Roles of the mammalian subventricular zone in brain development. Prog. Neurobiol. *69*, 49–69. https://doi.org/10.1016/s0301-0082(03)00002-9.
33. Martínez-Cerdeño, V., Cunningham, C.L., Camacho, J., Antczak, J.L., Prakash, A.N., Cziep, M.E., Walker, A.I., and Noctor, S.C. (2012). Comparative analysis of the subventricular zone in rat, ferret and macaque: evidence for an outer subventricular zone in rodents. PLoS One *7*, e30178. https://doi.org/10.1371/journal.pone.0030178.
34. Pollen, A.A., Nowakowski, T.J., Chen, J., Retallack, H., Sandoval-Espinosa, C., Nicholas, C.R., Shuga, J., Liu, S.J., Oldham, M.C., Diaz, A., et al. (2015). Molecular identity of human outer radial glia during cortical development. Cell *163*, 55–67. https://doi.org/10.1016/j.cell.2015.09.004.
35. Nowakowski, T.J., Pollen, A.A., Sandoval-Espinosa, C., and Kriegstein, A.R. (2016). Transformation of the Radial Glia Scaffold Demarcates Two Stages of Human Cerebral Cortex Development. Neuron *91*, 1219–1227. https://doi.org/10.1016/j.neuron.2016.09.005.
36. Liu, J.S. (2011). Molecular genetics of neuronal migration disorders. Curr. Neurol. Neurosci. Rep. *11*, 171–178. https://doi.org/10.1007/s11910-010-0176-5.
37. Rash, B.G., Duque, A., Morozov, Y.M., Arellano, J.I., Micali, N., and Rakic, P. (2019). Gliogenesis in the outer subventricular zone promotes enlargement and gyrification of the primate cerebrum. Proc. Natl. Acad. Sci. USA *116*, 7089–7094. https://doi.org/10.1073/pnas.1822169116.
38. Fietz, S.A., Kelava, I., Vogt, J., Wilsch-Bräuninger, M., Stenzel, D., Fish, J.L., Corbeil, D., Riehn, A., Distler, W., Nitsch, R., and Huttner, W.B. (2010). OSVZ progenitors of human and ferret neocortex are epithelial-like and expand by integrin signaling. Nat. Neurosci. *13*, 690–699. https://doi.org/10.1038/nn.2553.
39. Uchida, N., Buck, D.W., He, D., Reitsma, M.J., Masek, M., Phan, T.V., Tsukamoto, A.S., Gage, F.H., and Weissman, I.L. (2000). Direct isolation of human central nervous system stem cells. Proc. Natl. Acad. Sci. USA *97*, 14720–14725. https://doi.org/10.1073/pnas.97.26.14720.
40. Johnson, M.B., Wang, P.P., Atabay, K.D., Murphy, E.A., Doan, R.N., Hecht, J.L., and Walsh, C.A. (2015). Single-cell analysis reveals transcriptional heterogeneity of neural progenitors in human cortex. Nat. Neurosci. *18*, 637–646. https://doi.org/10.1038/nn.3980.
41. Chen, E.Y., Tan, C.M., Kou, Y., Duan, Q., Wang, Z., Meirelles, G.V., Clark, N.R., and Ma'ayan, A. (2013). Enrichr: interactive and collaborative HTML5

gene list enrichment analysis tool. BMC Bioinf. *14*, 128. https://doi.org/10.1186/1471-2105-14-128.

42. Kuleshov, M.V., Jones, M.R., Rouillard, A.D., Fernandez, N.F., Duan, Q., Wang, Z., Koplev, S., Jenkins, S.L., Jagodnik, K.M., Lachmann, A., et al. (2016). Enrichr: a comprehensive gene set enrichment analysis web server 2016 update. Nucleic Acids Res. *44*, W90–W97. https://doi.org/10.1093/nar/gkw377.

43. Xie, Z., Bailey, A., Kuleshov, M.V., Clarke, D.J.B., Evangelista, J.E., Jenkins, S.L., Lachmann, A., Wojciechowicz, M.L., Kropiwnicki, E., Jagodnik, K.M., et al. (2021). Gene Set Knowledge Discovery with Enrichr. Curr. Protoc. *1*, e90. https://doi.org/10.1002/cpz1.90.

44. Qi, Y., Cai, J., Wu, Y., Wu, R., Lee, J., Fu, H., Rao, M., Sussel, L., Rubenstein, J., and Qiu, M. (2001). Control of oligodendrocyte differentiation by the Nkx2.2 homeodomain transcription factor. Development *128*, 2723–2733. https://doi.org/10.1242/dev.128.14.2723.

45. Stolt, C.C., Lommes, P., Friedrich, R.P., and Wegner, M. (2004). Transcription factors Sox8 and Sox10 perform non-equivalent roles during oligodendrocyte development despite functional redundancy. Development *131*, 2349–2358. https://doi.org/10.1242/dev.01114.

46. Copray, S., Balasubramaniyan, V., Levenga, J., de Bruijn, J., Liem, R., and Boddeke, E. (2006). Olig2 overexpression induces the in vitro differentiation of neural stem cells into mature oligodendrocytes. Stem Cell. *24*, 1001–1010. https://doi.org/10.1634/stemcells.2005-0239.

47. Persengiev, S.P., Devireddy, L.R., and Green, M.R. (2002). Inhibition of apoptosis by ATFx: a novel role for a member of the ATF/CREB family of mammalian bZIP transcription factors. Genes Dev. *16*, 1806–1814. https://doi.org/10.1101/gad.992202.

48. Angelastro, J.M., Ignatova, T.N., Kukekov, V.G., Steindler, D.A., Stengren, G.B., Mendelsohn, C., and Greene, L.A. (2003). Regulated expression of ATF5 is required for the progression of neural progenitor cells to neurons. J. Neurosci. *23*, 4590–4600. https://doi.org/10.1523/jneurosci.23-11-04590.2003.

49. Angelastro, J.M., Mason, J.L., Ignatova, T.N., Kukekov, V.G., Stengren, G.B., Goldman, J.E., and Greene, L.A. (2005). Downregulation of activating transcription factor 5 is required for differentiation of neural progenitor cells into astrocytes. J. Neurosci. *25*, 3889–3899. https://doi.org/10.1523/jneurosci.3447-04.2005.

50. Arias, A., Lamé, M.W., Santarelli, L., Hen, R., Greene, L.A., and Angelastro, J.M. (2012). Regulated ATF5 loss-of-function in adult mice blocks formation and causes regression/eradication of gliomas. Oncogene *31*, 739–751. https://doi.org/10.1038/onc.2011.276.

51. Sheng, Z., Li, L., Zhu, L.J., Smith, T.W., Demers, A., Ross, A.H., Moser, R.P., and Green, M.R. (2010). A genome-wide RNA interference screen reveals an essential CREB3L2-ATF5-MCL1 survival pathway in malignant glioma with therapeutic implications. Nat. Med. *16*, 671–677. https://doi.org/10.1038/nm.2158.

52. Malone, C.D., Hasan, S.M.M., Roome, R.B., Xiong, J., Furlong, M., Opferman, J.T., and Vanderluit, J.L. (2012). Mcl-1 regulates the survival of adult neural precursor cells. Mol. Cell. Neurosci. *49*, 439–447. https://doi.org/10.1016/j.mcn.2012.02.003.

53. Widden, H., and Placzek, W.J. (2021). The multiple mechanisms of MCL1 in the regulation of cell fate. Commun. Biol. *4*, 1029. https://doi.org/10.1038/s42003-021-02564-6.

54. Jacobs, A.T., and Marnett, L.J. (2009). HSF1-mediated BAG3 expression attenuates apoptosis in 4-hydroxynonenal-treated colon cancer cells via stabilization of anti-apoptotic Bcl-2 proteins. J. Biol. Chem. *284*, 9176–9183. https://doi.org/10.1074/jbc.M808656200.

55. Boiani, M., Daniel, C., Liu, X., Hogarty, M.D., and Marnett, L.J. (2013). The stress protein BAG3 stabilizes Mcl-1 protein and promotes survival of cancer cells and resistance to antagonist ABT-737. J. Biol. Chem. *288*, 6980–6990. https://doi.org/10.1074/jbc.M112.414177.

56. Gentilella, A., and Khalili, K. (2010). BAG3 expression is sustained by FGF2 in neural progenitor cells and impacts cell proliferation. Cell Cycle *9*, 4245–4247. https://doi.org/10.4161/cc.9.20.13517.

57. Boyce, M., Bryant, K.F., Jousse, C., Long, K., Harding, H.P., Scheuner, D., Kaufman, R.J., Ma, D., Coen, D.M., Ron, D., and Yuan, J. (2005). A selective inhibitor of eIF2alpha dephosphorylation protects cells from ER stress. Science *307*, 935–939. https://doi.org/10.1126/science.1101902.

58. Torres-Peraza, J.F., Engel, T., Martín-Ibáñez, R., Sanz-Rodríguez, A., Fernández-Fernández, M.R., Esgleas, M., Canals, J.M., Henshall, D.C., and Lucas, J.J. (2013). Protective neuronal induction of ATF5 in endoplasmic reticulum stress induced by status epilepticus. Brain *136*, 1161–1176. https://doi.org/10.1093/brain/awt044.

59. Thomas, B., Eyssen, M., Peeters, R., Molenaers, G., Van Hecke, P., De Cock, P., and Sunaert, S. (2005). Quantitative diffusion tensor imaging in cerebral palsy due to periventricular white matter injury. Brain *128*, 2562–2577. https://doi.org/10.1093/brain/awh600.

60. Fan, G.G., Yu, B., Quan, S.M., Sun, B.H., and Guo, Q.Y. (2006). Potential of diffusion tensor MRI in the assessment of periventricular leukomalacia. Clin. Radiol. *61*, 358–364. https://doi.org/10.1016/j.crad.2006.01.001.

61. Zhou, J., Butler, E.E., and Rose, J. (2017). Neurologic Correlates of Gait Abnormalities in Cerebral Palsy: Implications for Treatment. Front. Hum. Neurosci. *11*, 103. https://doi.org/10.3389/fnhum.2017.00103.

62. Kinder, H.A., Baker, E.W., and West, F.D. (2019). The pig as a preclinical traumatic brain injury model: current models, functional outcome measures, and translational detection strategies. Neural Regen. Res. *14*, 413–424. https://doi.org/10.4103/1673-5374.245334.

63. Ballabh, P., and de Vries, L.S. (2021). White matter injury in infants with intraventricular haemorrhage: mechanisms and therapies. Nat. Rev. Neurol. *17*, 199–214. https://doi.org/10.1038/s41582-020-00447-8.

64. Pond, W.G., Boleman, S.L., Fiorotto, M.L., Ho, H., Knabe, D.A., Mersmann, H.J., Savell, J.W., and Su, D.R. (2000). Perinatal ontogeny of brain growth in the domestic pig. Proc. Soc. Exp. Biol. Med. *223*, 102–108. https://doi.org/10.1177/153537020022300114.

65. Liu, D.D., He, J.Q., Sinha, R., Eastman, A.E., Toland, A.M., Morri, M., Neff, N.F., Vogel, H., Uchida, N., and Weissman, I.L. (2023). Purification and characterization of human neural stem and progenitor cells. Cell *186*, 1179–1194.e15. https://doi.org/10.1016/j.cell.2023.02.017.

66. Etxeberria, A., Mangin, J.M., Aguirre, A., and Gallo, V. (2010). Adult-born SVZ progenitors receive transient synapses during remyelination in corpus callosum. Nat. Neurosci. *13*, 287–289. https://doi.org/10.1038/nn.2500.

67. Zhao, Y., Zhang, Y.D., Zhang, Y.Y., Qian, S.W., Zhang, Z.C., Li, S.F., Guo, L., Liu, Y., Wen, B., Lei, Q.Y., et al. (2014). p300-dependent acetylation of activating transcription factor 5 enhances C/EBPβ transactivation of C/EBPα during 3T3-L1 differentiation. Mol. Cell Biol. *34*, 315–324. https://doi.org/10.1128/mcb.00956-13.

68. Crowe, T.P., Greenlee, M.H.W., Kanthasamy, A.G., and Hsu, W.H. (2018). Mechanism of intranasal drug delivery directly to the brain. Life Sci. *195*, 44–52. https://doi.org/10.1016/j.lfs.2017.12.025.

69. Vaes, J.E.G., van Kammen, C.M., Trayford, C., van der Toorn, A., Ruhwedel, T., Benders, M.J.N.L., Dijkhuizen, R.M., Möbius, W., van Rijt, S.H., and Nijboer, C.H. (2021). Intranasal mesenchymal stem cell therapy to boost myelination after encephalopathy of prematurity. Glia *69*, 655–680. https://doi.org/10.1002/glia.23919.

70. Borgonetti, V., and Galeotti, N. (2023). Posttranscriptional Regulation of Gene Expression Participates in the Myelin Restoration in Mouse Models of Multiple Sclerosis: Antisense Modulation of HuR and HuD ELAV RNA Binding Protein. Mol. Neurobiol. *60*, 2661–2677. https://doi.org/10.1007/s12035-023-03236-8.

71. Sharifian, A., Varshosaz, J., Aliomrani, M., and Kazemi, M. (2023). Nose to brain delivery of ibudilast micelles for treatment of multiple sclerosis in an experimental autoimmune encephalomyelitis animal model. Int. J. Pharm. *638*, 122936. https://doi.org/10.1016/j.ijpharm.2023.122936.

72. Baker, R., Esquenazi, A., Benedetti, M.G., and Desloovere, K. (2016). Gait analysis: clinical facts. Eur. J. Phys. Rehabil. Med. *52*, 560–574.

73. Kessel, D. (2006). Protection of Bcl-2 by salubrinal. Biochem. Biophys. Res. Commun. *346*, 1320–1323. https://doi.org/10.1016/j.bbrc.2006.06.056.

74. Balakrishnan, B., Siddiqi, A., Mella, J., Lupo, A., Li, E., Hollien, J., Johnson, J., and Lai, K. (2019). Salubrinal enhances eIF2α phosphorylation and improves fertility in a mouse model of Classic Galactosemia. Biochim. Biophys. Acta, Mol. Basis Dis. *1865*, 165516. https://doi.org/10.1016/j.bbadis.2019.07.010.

75. Wei, J., Zhang, W., Li, J., Jin, Y., and Qiu, Z. (2022). Application of the transgenic pig model in biomedical research: A review. Front. Cell Dev. Biol. *10*, 1031812. https://doi.org/10.3389/fcell.2022.1031812.

76. Schindelin, J., Arganda-Carreras, I., Frise, E., Kaynig, V., Longair, M., Pietzsch, T., Preibisch, S., Rueden, C., Saalfeld, S., Schmid, B., et al. (2012). Fiji: an open-source platform for biological-image analysis. Nat. Methods *9*, 676–682. https://doi.org/10.1038/nmeth.2019.

77. Love, M.I., Huber, W., and Anders, S. (2014). Moderated estimation of fold change and dispersion for RNA-seq data with DESeq2. Genome Biol. *15*, 550. https://doi.org/10.1186/s13059-014-0550-8.

78. Ge, S.X., Son, E.W., and Yao, R. (2018). iDEP: an integrated web application for differential expression and pathway analysis of RNA-Seq data. BMC Bioinf. *19*, 534. https://doi.org/10.1186/s12859-018-2486-6.

79. Chen, S., Zhou, Y., Chen, Y., and Gu, J. (2018). fastp: an ultra-fast all-in-one FASTQ preprocessor. Bioinformatics *34*, i884–i890. https://doi.org/10.1093/bioinformatics/bty560.

80. Bray, N.L., Pimentel, H., Melsted, P., and Pachter, L. (2016). Near-optimal probabilistic RNA-seq quantification. Nat. Biotechnol. *34*, 525–527. https://doi.org/10.1038/nbt.3519.

81. Soneson, C., Love, M.I., and Robinson, M.D. (2015). Differential analyses for RNA-seq: transcript-level estimates improve gene-level inferences. F1000Res. *4*, 1521. https://doi.org/10.12688/f1000research.7563.2.

82. Reid, J.L., Dawson, D., and Macrae, I.M. (1995). Endothelin, cerebral ischaemia and infarction. Clin. Exp. Hypertens. *17*, 399–407. https://doi.org/10.3109/10641969509087080.

83. Virley, D., Hadingham, S.J., Roberts, J.C., Farnfield, B., Elliott, H., Whelan, G., Golder, J., David, C., Parsons, A.A., and Hunter, A.J. (2004). A new primate model of focal stroke: endothelin-1-induced middle cerebral artery occlusion and reperfusion in the common marmoset. J. Cereb. Blood Flow Metab. *24*, 24–41. https://doi.org/10.1097/01.Wcb.0000095801.98378.4a.

84. Wang, Y., Jin, K., and Greenberg, D.A. (2007). Neurogenesis associated with endothelin-induced cortical infarction in the mouse. Brain Res. *1167*, 118–122. https://doi.org/10.1016/j.brainres.2007.06.065.

85. Tennant, K.A., and Jones, T.A. (2009). Sensorimotor behavioral effects of endothelin-1 induced small cortical infarcts in C57BL/6 mice. J. Neurosci. Methods *181*, 18–26. https://doi.org/10.1016/j.jneumeth.2009.04.009.

86. Faiz, M., Sachewsky, N., Gascón, S., Bang, K.W.A., Morshead, C.M., and Nagy, A. (2015). Adult Neural Stem Cells from the Subventricular Zone Give Rise to Reactive Astrocytes in the Cortex after Stroke. Cell Stem Cell *17*, 624–634. https://doi.org/10.1016/j.stem.2015.08.002.

87. Gilmour, G., Iversen, S.D., O'Neill, M.F., and Bannerman, D.M. (2004). The effects of intracortical endothelin-1 injections on skilled forelimb use: implications for modelling recovery of function after stroke. Behav. Brain Res. *150*, 171–183. https://doi.org/10.1016/j.bbr.2003.07.006.

88. Dhari, Z., Leonetti, C., Lin, S., Prince, A., Howick, J., Zurakowski, D., Wang, P.C., Jonas, R.A., and Ishibashi, N. (2021). Impact of Cardiopulmonary Bypass on Neurogenesis and Cortical Maturation. Ann. Neurol. *90*, 913–926. https://doi.org/10.1002/ana.26235.

89. Saikali, S., Meurice, P., Sauleau, P., Eliat, P.A., Bellaud, P., Randuineau, G., Vérin, M., and Malbert, C.H. (2010). A three-dimensional digital segmented and deformable brain atlas of the domestic pig. J. Neurosci. Methods *192*, 102–109. https://doi.org/10.1016/j.jneumeth.2010.07.041.

90. Batie, M., Frost, J., Frost, M., Wilson, J.W., Schofield, P., and Rocha, S. (2019). Hypoxia induces rapid changes to histone methylation and reprograms chromatin. Science *363*, 1222–1226. https://doi.org/10.1126/science.aau5870.

91. Mittal, D., Ali, A., Md, S., Baboota, S., Sahni, J.K., and Ali, J. (2014). Insights into direct nose to brain delivery: current status and future perspective. Drug Deliv. *21*, 75–86. https://doi.org/10.3109/10717544.2013.838713.

92. Kuboyama, K., Fujikawa, A., Suzuki, R., and Noda, M. (2015). Inactivation of Protein Tyrosine Phosphatase Receptor Type Z by Pleiotrophin Promotes Remyelination through Activation of Differentiation of Oligodendrocyte Precursor Cells. J. Neurosci. *35*, 12162–12171. https://doi.org/10.1523/JNEUROSCI.2127-15.2015.

93. Webb, R.L., Kaiser, E.E., Jurgielewicz, B.J., Spellicy, S., Scoville, S.L., Thompson, T.A., Swetenburg, R.L., Hess, D.C., West, F.D., and Stice, S.L. (2018). Human Neural Stem Cell Extracellular Vesicles Improve Recovery in a Porcine Model of Ischemic Stroke. Stroke *49*, 1248–1256. https://doi.org/10.1161/strokeaha.117.020353.

94. Kinder, H.A., Baker, E.W., Howerth, E.W., Duberstein, K.J., and West, F.D. (2019). Controlled Cortical Impact Leads to Cognitive and Motor Function Deficits that Correspond to Cellular Pathology in a Piglet Traumatic Brain Injury Model. J. Neurotrauma *36*, 2810–2826. https://doi.org/10.1089/neu.2019.6405.

95. Kinder, H.A., Baker, E.W., Wang, S., Fleischer, C.C., Howerth, E.W., Duberstein, K.J., Mao, H., Platt, S.R., and West, F.D. (2019). Traumatic Brain Injury Results in Dynamic Brain Structure Changes Leading to Acute and Chronic Motor Function Deficits in a Pediatric Piglet Model. J. Neurotrauma *36*, 2930–2942. https://doi.org/10.1089/neu.2018.6303.

STAR★METHODS

KEY RESOURCES TABLE

REAGENT or RESOURCE	SOURCE	IDENTIFIER
Antibodies		
Chicken polyclonal anti-Vimentin	Millipore	Cat# AB5733; RRID:AB_11212377
Mouse monoclonal anti-Vimentin	Sigma-Aldrich	Cat# V6630; RRID:AB_477627
Rabbit polyclonal anti-Sox2	Millipore	Cat# AB5603; RRID:AB_2286686
Rabbit polyclonal anti-Sox2	Cell Signaling	Cat# 2748; RRID:AB_823640
Mouse monoclonal anti-Sox2	Santa Cruz	Cat# sc-365823; RRID:AB_10842165
Rabbit anti-CD133	Abcam	Cat# ab19898; RRID:AB_470302
Mouse monoclonal anti-Mash1	BD Biosciences	Cat# 556604; RRID:AB_396479
Rabbit monoclonal anti-PDGFRα	Cell Signaling	Cat# 3174; RRID:AB_2162345
Mouse monoclonal anti-ki67	BD Biosciences	Cat# 550609; RRID:AB_393778
Guinea pig anti-Doublecortin	Millipore	Cat# AB2253; RRID:AB_1586992
Rabbit polyclonal anti-Iba1	FUJIFILM Wako Pure Chemical	Cat# 019–19741; RRID:AB_839504
Mouse monoclonal anti-Olig2	Millipore	Cat# MABN50; RRID:AB_10807410
Rabbit polyclonal anti-Olig2	Millipore	Cat# AB9610; RRID:AB_570666
Goat polyclonal anti-Olig2	R&D System	Cat# AF2418; RRID:AB_2157554
Rabbit polyclonal anti-Olig1	Abcam	Cat# ab68105; RRID:AB_1142042
Mouse monoclonal anti-CC1	Millipore	Cat# OP80; RRID:AB_2057371
Mouse monoclonal anti-MBP	Thermo Fisher Scientific	Cat# MA1-24988; RRID:AB_794985
Rabbit polyclonal anti-GLAST (EAAT1)	Abcam	Cat# ab416; RRID:AB_304334
Mouse monoclonal anti-Nkx2.2	DSHB	Cat# 74.5A5; RRID:AB_531794
Rabbit polyclonal anti-HOPX	Atlas	Cat# HPA030180; RRID:AB_10603770
Mouse monoclonal anti-HOPX	Santa Cruz	Cat# sc-398703; RRID:AB_2687966
Chicken polyclonal anti-GFP	Abcam	Cat# ab13970; RRID:AB_300798
Rabbit Neurofilament 200	Thermo Fisher Scientific	Cat# ICN697051; RRID:AB_2335157
Mouse monoclonal SMI-32	BioLegend	Cat# 801701; RRID:AB_2564642
Goat polyclonal eIF2α	Rockland	Cat# 600-101-ML7
Rabbit monoclonal phospho-EIF2α (Ser51)	Cell signaling	Cat# 3597; RRID:AB_390740
Mouse monoclonal GFAP	Abcam	Cat# ab4648; RRID:AB_449329
Mouse anti-GLAST-PE	Miltenyi Biotec	Cat# 130-118-483; RRID:AB_2733723
Rabbit monoclonal anti-NG2	abcam	Cat# ab275024; RRID:AB_2922401
Mouse monoclonal anti-MBP	Santa Cruz	Cat# sc-271524; RRID:AB_10655672
Hoechst 33342	Thermo Fisher Scientific	Cat# 62249
Donkey anti-Mouse IgG (H + L) Highly Cross-Adsorbed Secondary Antibody, Alexa Fluor 488	Invitrogen	Cat# A-21202; RRID:AB_141607
Donkey anti-Rabbit IgG (H + L) Highly Cross-Adsorbed Secondary Antibody, Alexa Fluor 488	Invitrogen	Cat# A-21206; RRID:AB_2535792
Donkey anti-Goat IgG (H + L) Cross-Adsorbed Secondary Antibody, Alexa Fluor 488	Invitrogen	Cat# A-11055; RRID:AB_2534102
Donkey anti-Chicken IgY (H + L) Highly Cross Adsorbed Secondary Antibody, Alexa Fluor 488	Invitrogen	Cat# A78948; RRID:AB_2921070
Donkey anti-Mouse IgG (H + L) Highly Cross-Adsorbed Secondary Antibody, Alexa Fluor 555	Invitrogen	Cat# A-31570; RRID:AB_2536180
Donkey anti-Rabbit IgG (H + L) Highly Cross-Adsorbed Secondary Antibody, Alexa Fluor 555	Invitrogen	Cat# A-31572; RRID:AB_162543
Donkey anti-Goat IgG (H + L) Cross-Adsorbed Secondary Antibody, Alexa Fluor 555	Invitrogen	Cat# A-21432; RRID:AB_2535853

(*Continued on next page*)

Continued

REAGENT or RESOURCE	SOURCE	IDENTIFIER
Goat anti-Guinea Pig IgG (H + L) Highly Cross-Adsorbed Secondary Antibody, Alexa Fluor 555	Invitrogen	Cat# A-21435; RRID:AB_2535856
Donkey anti-Mouse IgG (H + L) Highly Cross-Adsorbed Secondary Antibody, Alexa Fluor 647	Invitrogen	Cat# A-31571; RRID:AB_162542
Donkey anti-Rabbit IgG (H + L) Highly Cross-Adsorbed Secondary Antibody, Alexa Fluor 647	Invitrogen	Cat# A-31573; RRID:AB_2536183
Donkey anti-Goat IgG (H + L) Cross-Adsorbed Secondary Antibody, Alexa Fluor 633	Invitrogen	Cat# A-21082; RRID:AB_2535739
Donkey anti-Chicken IgY (H + L) Highly Cross Adsorbed Secondary Antibody, Alexa Fluor 647	Invitrogen	Cat# A-78952; RRID:AB_2921074
Biotin-SP (long spacer) AffiniPure F(ab')2 Fragment Donkey Anti-Rabbit IgG (H + L)	Jackson ImmunoResearch	Cat# 711-066-152; RRID:AB_2340594
Biotin-SP (long spacer) AffiniPure Donkey Anti-Mouse IgG (H + L)	Jackson ImmunoResearch	Cat# 715-065-150; RRID:AB_2307438
Alexa Fluor 488 AffiniPure Fab Fragment Donkey Anti-mouse IgG (H + L)	Jackson ImmunoResearch	Cat# 715-547-003; RRID:AB_2340851
Bacterial and virus strains		
Ad-GFP	Vector Biolabs	Cat# 1060
Biological samples		
Human infant brain tissue	NIH NeuroBioBank	Table S1; https://neurobiobank.nih.gov/
Human adult brain tissue	NIH NeuroBioBank	Table S1; https://neurobiobank.nih.gov/
Chemicals, peptides, and recombinant proteins		
Sorafenib tosylate	Sigma-Aldrich	Cat# SML2633
Salubrinal	Sigma-Aldrich	Cat# SML0951
endothelin-1	Millipore	Cat# 05-23-3800
Isoflurane	Covertus	Cat# 11695067772
Fentanyl	Hikma	Cat# 0641-6030
Rocuronium	Phlow	Cat# 81565-204-02
Cefazolin	WG Critical Care	Cat# 44567-707-25
Ketamine	Dechra veterinary products	Cat# ANADA200-073
Xylazine	Covertus	Cat# 1XYL006
RNAscope Protease Plus	Advanced Cell Diagnostics	Cat# 322331
Blocking reagent	Akoya Biosciences	Cat# FP1012
VECTASHIELD mounting medium with DAPI	Vector Laboratories	Cat# H-1200; RRID:AB_2336790
TSA Plus Fluorescein Kit	Akoya Biosciences	Cat# NEL741001KT
TSA Plus Cyanine 3 Kit	Akoya Biosciences	Cat# NEL744001KT
Streptavidin-HRP	Akoya Biosciences	Cat# NEL750001EA; RRID:AB_2617185
TrypLE Express Enzyme (1X), phenol red	Gibco	Cat# 12605010
DNase	Worthington	Cat# LK003170
Trypan blue solution	Sigma-Aldrich	Cat# T8154
SYTOX Red Dead Cell Stain for 633 or 635 nm excitation	Invitrogen	Cat# S34859
Nonidet P40 Substitute	Sigma	Cat# 74385
RNase Inhibitor	Millipore	Cat# 3335399001
Nuclease-Free Water	Thermo Fisher Scientific	Cat# AM9932
Papain Dissociation System	Worthington	Cat# LK003150
KnockOut DMEM/F-12	ThermoFisher	Cat# 12660012
GlutaMAX Supplement	ThermoFisher	Cat# 35050061
N-2 Supplement	ThermoFisher	Cat# 17502001

(*Continued on next page*)

Continued

REAGENT or RESOURCE	SOURCE	IDENTIFIER
PDGF-AA	Fujifilm Wako	Cat# 169-19733
Biotin	Millipore	Cat# B4501
Thyronine	Millipore	Cat# T2877
Thyroxine	Millipore	Cat# T2376
Critical commercial assays		
ApopTag Fluorescein *In Situ* Apoptosis Detection Kit	Millipore	Cat# S7110; RRID:AB_2661855
RNAscope Multiplex Fluorescent Reagent Kit V2	Advanced Cell Diagnostics	Cat# 323100
Absolutely RNA Nanoprep Kit	Agilent	Cat# 400753
RNA 6000 Pico Kit	Agilent	Cat# 5067-1513
High Sensitivity DNA Kit	Agilent	Cat# 5067-4626
RNAscope Probe-Hs-MKI67-C2	Advanced Cell Diagnostics	Cat# 591771-C2
RNAscope Probe-Hs-HOPX	Advanced Cell Diagnostics	Cat# 423001
RNAscope Probe-Hs-ATF5-C2	Advanced Cell Diagnostics	Cat# 496661-C2
RNAscope Probe-Hs-MCL1-O1-C3	Advanced Cell Diagnostics	Cat# 1109481-C3
RNAscope Probe-Ss-MCL1-C2	Advanced Cell Diagnostics	Cat# 1143421-C2
RNAscope Probe-Ss-ATF5-C1	Advanced Cell Diagnostics	Cat# 1143411-C1
RNAscope Probe-Ss-BAG3-C2	Advanced Cell Diagnostics	Cat# 1143541-C2
RNAscope Probe-Ss-BCL2A1-C2	Advanced Cell Diagnostics	Cat# 1143451-C2
Deposited data		
RNA-sequencing data	This paper	NCBI Sequence Read Archive (NCBI: PRJNA992775)
Mendeley dataset	This paper	https://doi.org/10.17632/wc2ts3r6dd.1
Experimental models: Organisms/strains		
Yorkshire piglets	Archer Farm	http://www.archerfarmsinc.com/
Mouse ICR	Japan SLC	N/A
Software and algorithms		
ImageJ (FIJI)	Schindelin et al.[76]	https://imagej.net/software/fiji/; RRID:SCR_002285
Neurolucida	MBF Bioscience	https://www.mbfbioscience.com/products/neurolucida/; RRID:SCR_001775
DeSeq2 package for R (iDEP, version 93)	Love et al.[77] and Ge et al.[78]	http://bioinformatics.sdstate.edu/idep93/
Enrichr	Chen et al.[41]; Kuleshov et al.[42] and Xie et al.[43]	https://maayanlab.cloud/Enrichr/; RRID:SCR_001575
FlowJo	Tree Star, Inc.	https://www.flowjo.com/; RRID:SCR_008520;
Ovation SoLo RNA-Seq System	NuGEN Tecan Genomics	Cat# 0500
fastp (version 0.20.1)	Chen et al.[79]	https://github.com/OpenGene/fastp; RRID:SCR_016962
bcl2fastq (version 2.18.0.12)	Illumina	https://support.illumina.com/downloads/bcl2fastq-conversion-software-v2-20.html; RRID:SCR_015058
Kallisto (version 0.46.2)	Bray et al.[80]	https://pachterlab.github.io/kallisto/; RRID:SCR_016582
tximport (version 1.18.0)	Soneson et al.[81]	https://bioconductor.org/packages/release/bioc/html/tximport.html; RRID:SCR_016752
Tolerably Obsessive Registration and Tensor Optimization Indolent Software Ensemble (TORTOISE) software package	NIH	https://tortoise.nibib.nih.gov/; RRID:SCR_001645
DTI Studio	MRI Studio; Johns Hopkins University	https://www.mristudio.org/; RRID:SCR_001398

(Continued on next page)

Continued

REAGENT or RESOURCE	SOURCE	IDENTIFIER
ROIEditor	MRI Studio; Johns Hopkins University	https://www.mristudio.org/; RRID:SCR_001398
GraphPad Prism 10 (version 10.1.2)	GraphPad	https://www.graphpad.com
Other		
iE33 xMARTRIX Ultrasound system	Philips	iE33
Removable needle syringe 50μL	Hamilton	Cat# 80530
Small Hub removable needles 26s ga	Hamilton	Cat# 7758-02
Small Hub removable needles 28 ga	Hamilton	Cat# 7803-02
Tissue-Tek O.C.T. Compound	Sakura Finetek	Cat# 4583
MAD intranasal mucosal atomization device	Teleflex	Cat# MAD100
Cell strainer 40 μm Nylon	BD Biosciences	Cat# 352340
NovaSeq 6000 Sequence System	Illumina	Cat# 20012850; RRID:SCR_016387
GAITFour system	CIR system Inc.	https://www.gait4dog.com/

EXPERIMENTAL MODEL AND STUDY PARTICIPANT DETAILS

Human brain tissue samples

Human cerebral tissue specimens were obtained from the National Institutes of Health (NIH) NeuroBioBank (request ID #1422 and #1665). A total of twenty fixed human tissue specimens (infant control: *n* = 6, infant injury: *n* = 4, adult control: *n* = 5, adult injury: *n* = 5) were used in this study (Table S1). Infant donors were less than 5 months after birth. Brains whose neuropathology diagnosis was hypoxic ischemic encephalopathy, ischemia, stroke, or cerebral infarction were used as the injured brains. Brains whose neuropathology reports showed no unremarkable findings were used as the control brains. Cases in which major congenital anomalies or known genetic diagnoses were recorded were excluded. Sample sizes for experiments were determined according to a previous study.[24] There were no significant differences in average age between the infant control and the infant injury groups, and between the adult control and the adult injury groups (unpaired t-test).

Animals

A total of 68 female Yorkshire piglets (Archer Farms, Inc., Darlington, MD) were used in this study. Female piglets were randomly assigned to experimental groups. Piglets were housed in cages in a controlled environment (24 ± 1°C, 12 h light/dark cycle changed 6:00 o'clock) with a nutritionally balanced milk formula (OptiLac Baby Pig Milk Replacer, Hubbard) in a domestic animal colony of Comparative Medicine Unit at Children's National Hospital). At 3–4 weeks of age, piglets were weaned from milk and provided with dry chow (Tekland laboratory diet, Envigo) and water *ad libitum*. All experiments were performed in compliance with the guidelines of the National Institutes of Health "Guide for the Care and Use of Laboratory Animals," and were approved by the Institutional Animal Care and Use Committee (IACUC) of the Children's National Hospital (protocol #30593).

All of the experiments involving live mice were performed in accordance with the guidelines and regulations of Nagoya City University and approved by the President of Nagoya City University (protocol #21–028). Mice were housed in cages lined up with chip bedding in a controlled environment (23 ± 1°C, 12 h light/dark cycle changed 08:00 o'clock) with *ad libitum* access to water and food (MF, Oriental Yeast, Tokyo, Japan) in a specific-pathogen-free facility. Wild-type (WT) Institute for Cancer Research (ICR) mice were purchased from Japan SLC (Shizuoka, Japan). Before delactation, littermates were housed with their mother or foster mouse. In all experiments using mice, both male and female healthy mice were used. Littermates were randomly assigned to experimental groups.

METHOD DETAILS

Preparation for piglet surgery

As previously described,[23,24] animals were sedated with intramuscular ketamine and xylazine, and intubated with 3.0–4.0 cuffed endotracheal tube. Each animal was ventilated at a fraction of inspired oxygen of 0.21, and a rate of 12–20 breaths/min, a peak inspiratory pressure of 20 torr, and a positive end expiratory pressure of 3 torr, by means of a pressure control ventilator (Servo Ventilator 300; Siemens, New York, NY). Intravenous bolus injections of fentanyl, rocuronium, and cefazolin via a peripheral intravenous line were administered before surgery. Anesthesia was maintained by a continuous inhalant isoflurane and infusion of fentanyl and rocuronium throughout the entire experiment. Mean and systolic blood pressure, heart rate, SpO2, and rectal temperature were monitored continuously throughout each experiment and recorded every 15 min.

In vivo cell labeling

All surgical procedures were performed under sterile conditions. Two-week-old piglets were positioned and secured into a stereotaxic frame to prevent movement and ensure that the brain was on a level plane. A skin incision was made on the rostral-caudal axis to expose the skull. A lightweight, electrical drill was used to remove a portion of the skull to expose the parietal cerebral cortex. An ultrasound system (iE33 xMARTRIX, Philips) was used to locate the injection site (the OSVZ region, and the lateral ventricle as ISVZ) and guide the needle with real-time imaging during insertion. A 28-gauge Hamilton syringe (Hamilton Company) was used to inject 15 μL of Ad-CMV-GFP (Vector Biolabs). Either the ISVZ or the OSVZ region in the anterior SVZ was labeled. It is possible that vertical injection of adenoviral suspension can directly label not only the SVZ cells, but also dorsal periventricular white matter above the SVZ. Thus, the needle was inserted diagonally at an angle of 28° from vertical line to the surface of the cerebral cortex, in order to avoid the potential direct labeling of the injured area. Furthermore, the adenoviral suspension was injected for 10 min, and the needle was left in place for 10 min before being slowly withdrawn. To label neural stem cells in the ISVZ, the adenoviral suspension was injected into the lateral ventricle. These procedures were performed before the injection of endothelin-1, and reproducibly labeled cells in either the ISVZ or the OSVZ.

Brain injury

Endothelin-1 is a potent vasoconstrictor and intracortical injection of endothelin-1 into animal brains causes an ischemic lesion not only in rodents, but also in primates.[82–86] We modified the endothelin-1 ischemic brain injury model for piglet based on previous studies.[84–86] As described above, the parietal cerebral cortex of a 2-week-old piglet was exposed under sterile condition. A 1 μg/μL solution of endothelin-1 (Millipore) dissolved in sterile saline was used.[87] An ultrasound system was used to locate the injection site and guide the needle with real-time imaging during insertion. A 26-gauge Hamilton syringe was used to inject 25 μL of endothelin-1 solution into dorsal periventricular white matter (superior corona radiata) above the anterior SVZ, over the course of 10 min. The needle was left in place for 5 min following injection to prevent leakage from the region of interest through space around the needle, and then slowly withdrawn. Following injection, the dura was sutured, and a sterilized plate was used to close the skull opening. The scalp was sutured, and animals were allowed to recover and carefully monitored during the recovery period. This procedure reproducibly yielded focal ischemic lesions at dorsal periventricular white matter region above the anterior SVZ.

Tissue harvest

As previously described,[23,24] animals were anesthetized and transarterially perfused through the common carotid artery. Transarterial perfusion with 500 mL of saline was followed by 500 mL of 4% paraformaldehyde in 0.1 M PBS (pH 7.4). Brains were removed and further post-fixed at 4°C in a 4% paraformaldehyde solution in 0.1 M PBS. For post-fixed 6-week-old piglet brains, diffusion tensor imaging was performed before the subsequent processes. Brains were then cut into smaller tissue blocks. Tissue blocks were cryoprotected in a 15% sucrose solution in 0.1 M PBS for 24 h at 4°C, followed by incubation in a 30% sucrose solution in 0.1 M PBS for 48–72 h at 4°C. All samples were embedded in O.C.T. compound (Sakura FineTek). Serial 16-, 20- or 50-μm-thick coronal cerebral brain sections were collected using a cryostat at −20°C. Tissue sections were stored at −80°C until further processing.

Immunohistochemistry

Immunohistochemistry was performed as described previously.[24,88] For pig tissue, coronal sections were incubated for 1 h at room temperature (RT) in 20% normal donkey serum in carrier solution (1% bovine serum albumin, 1% normal donkey serum, and 0.3% Triton X- in 0.1 M PBS). Sections were then incubated in primary antibodies, diluted in carrier solution overnight at 4°C. Alexa Fluor-conjugated secondary antibodies (1:500, Invitrogen) were diluted in carrier solution and applied to sections for 2 h at RT. For signal amplification, 1% H2O2 in PBS was applied to tissue sections for 30 min at RT, and biotinylated secondary antibodies (1:500, Jackson ImmunoResearch Laboratory Inc.) and streptavidin-horseradish peroxidase (1:2000, Akoya Biosciences) were used. The signals were visualized using the TSA Fluorescence System (1:500, Akoya Biosciences) for 5 min at RT. For double staining using anti-Sox2 and anti-Ki67 antibodies, sequential immunostaining was performed with AffiniPure Fab Fragment Donkey Anti-mouse IgG (H + L) (Jackson ImmunoResearch Laboratories, Inc.) was used. The following primary antibodies were used: chicken anti-Vimentin (1:1,000; Millipore RRID:AB_11212377), mouse anti-Vimentin (1:1000, Sigma RRID:AB_477627), rabbit anti-Sox2 (1:500, Millipore RRID:AB_2286686, 1:200, Cell Signaling RRID:AB_823640), mouse anti-Sox2 (1:200, Santa Cruz RRID:AB_10842165), rabbit anti-CD133 (1:100, abcam RRID:AB_470302), mouse anti-Mash1 (1:200, BD Biosciences RRID:AB_396479), rabbit anti-PDGFRα (1:50, Cell Signaling RRID:AB_2162345), mouse anti-ki67 (1:200; BD Biosciences RRID:AB_393778), guinea pig anti-Doublecortin (1:1,000; Millipore RRID:AB_1586992), rabbit anti-Iba1 (1:1,000, Wako RRID:AB_839504), mouse anti-Olig2 (1:250, Millipore RRID:AB_10807410), rabbit anti-Olig2 (1:200, Millipore RRID:AB_570666), goat anti-Olig2 (1:100, R&D RRID:AB_2157554), rabbit anti-Olig1 (1:100, abcam RRID:AB_1142042), mouse anti-CC1 (1:400, Millipore RRID:AB_2057371), mouse anti-MBP (1:50, Invitrogen RRID:AB_794985), rabbit anti-GLAST (1:100, abcam RRID:AB_304334), mouse anti-Nkx2.2 (1:100, DSHB RRID:AB_531794), rabbit anti-HOPX (1:500, Atlas RRID:AB_10603770), mouse anti-HOPX (1:50, Santa Cruz RRID:AB_2687966), chicken anti-GFP (1:500, abcam RRID:AB_300798), rabbit Neurofilament 200 (1:500, ThermoFisher RRID:AB_2335157), mouse SMI-32 (1:500, BioLegend RRID:AB_2564642), rabbit *p*-EIF2α (Ser51) (1:500, Cell Signaling RRID:AB_390740) and goat EIF2α (1:500, Rockland Cat# 600-101-ML7). Sections were mounted with VECTASHIELD mounting medium for fluorescence with DAPI (Vector Laboratories, Inc.). For the Terminal deoxynucleotidyl transferase-mediated biotinylated UTP nick end labeling (TUNEL) assays, ApopTag

Fluorescein *In Situ* Apoptosis Detection Kit (Millipore) was used following the manufacturer's instructions except the protein kinase process was performed using Protease plus reagent (Advanced Cell Diagnostics) at 37°C for 30 min.

For human tissue, all methods were performed in accordance with the guidelines and regulations of Children's National Hospital and Children's National Research Institute. Tissue blocks were cryoprotected and cut into 14-, 20- or 50-μm-thick coronal sections on a cryostat. Antigen retrieval was performed with 10 mM Na Citrate buffer (pH 6.0) at 95°C for 10 min. Following antigen retrieval, slides were washed with 0.2% Triton X- in PBS, placed in 3% H2O2 in 0.2% Triton X- in PBS for 45 min at RT, and then blocked with TNB solution (0.5% blocking reagent (Akoya Biosciences) in 0.1 M Tris-HCl, pH 7.6) at RT for 1 h. Sections were incubated in primary antibodies diluted in TNB solution overnight at 4°C, and in biotinylated secondary antibodies for 2 h at RT. Sections were then incubated for 30 min in streptavidin-horseradish peroxidase that was diluted with TNB. Sections were incubated using TSA Fluorescence System (1:500) for 5 min at RT, and then rinsed with 0.3% Triton X- in 0.1 M PBS. The following primary antibodies were used: chicken anti-Vimentin (1:500; Millipore RRID:AB_11212377), mouse anti-Mash1 (1:100, BD Biosciences RRID:AB_396479), mouse anti-ki67 (1:200; BD Biosciences RRID:AB_393778), goat anti-Olig2 (1:100, R&D RRID:AB_2157554), mouse anti-CC1 (1:200, Millipore RRID:AB_2057371), rabbit anti-Iba1 (1:1,000, Wako RRID:AB_839504) and mouse GFAP (1:500, Abcam RRID:AB_449329). Sections were mounted with VECTASHIELD mounting medium for fluorescence with DAPI (Vector Laboratories, Inc.).

All images were acquired using an Olympus FV1000 confocal microscope or an LSM 700 confocal laser-scanning microscope (Carl Zeiss, Jena, TH, Germany) with a 10x, 20x or 40x objective lens. The morphology of Vimentin$^+$ radial glial cells was reconstructed using Neurolucida (MBF Bioscience).

RNAscope *in situ* hybridization

Tissue was collected and processed using the standard procedures described above. For piglet tissue, 16 μm-thick cryosections were collected and stored at −80°C prior to use. The RNAscope Multiplex Fluorescent Reagent Kit V2 (Advanced Cell Diagnostics) was used to perform fluorescent labeling of different RNA molecules according to the manufacturer's instruction with the following changes: Protease plus reagent at 37°C for 30 min. No target retrieval step was performed. RNAscope probes used were: *Atf5*, *Mcl1*, *Bag3*. Cells with at least two fluorescent puncta were counted as positive for that probe.

For human tissue, 14 μm-thick cryosections were collected and stored at −80°C prior to use. The RNAscope Multiplex Fluorescent Reagent Kit V2 was used for fluorescent labeling as described above. The target retrieval step was performed for 5 min at 96°C–100°C. RNAscope probes of *Hopx*, *MKi67, Atf5,* and *Mcl1* were used. Cells with at least one fluorescent punctum were counted as positive for that probe. Images were acquired using an Olympus FV1000 confocal microscope with a 40× objective lens.

Cellular analysis

Coronal sections of the brain were used for immunohistochemistry and RNAscope analysis of the SVZ and white matter above the SVZ. Since we previously demonstrated that the anterior part of the SVZ displays the highest density/number of proliferating progenitor cells and resembles its human counterpart,[24] we focused our analysis on the anterior SVZ. As previously described, the anterior SVZ was divided into the following two subregions: dorsolateral and lateral.[88] The sharp boundary between ISVZ and OSVZ was identified based on cell density in DAPI-stained tissue, as previously described.[33] Briefly, the cell dense region surrounding the lateral ventricle includes the ISVZ. A lower density zone compared to the ISVZ, but at a higher cell density than the overlying cortical white matter, is the OSVZ. Depending on the size of the SVZ, a total of 3–8 images were acquired from separate microscopic fields at 40x in 1 μm intervals with an Olympus confocal microscope or an LSM 700 confocal laser-scanning microscope. All images were processed and quantified using Fiji ImageJ software.[76] The length of Vimentin$^+$ processes in the anterior SVZ was also measured and averaged using Fiji ImageJ software in separate microscopic fields at 40x with a confocal microscope. The cellular analysis within the periventricular white matter was performed separately (more than 8 images per region at 40x in 1 μm intervals), based on the anatomical atlas and functional cortical map of the porcine brain.[89] The intensity of CD133 expression in DAPI$^+$ cells was measured using Fiji ImageJ software.[90] For quantification of GFP$^+$ cells, 4 images were acquired from the anterior SVZ at 40x in 1 μm intervals. For identification and quantification of GFP$^+$ cells on the plane of the injection site, co-labeling with the following markers was used: Doublecortin, Olig2, Sox2, and HOPX. Percentages were generated from separate immunostains and therefore do not add up to exactly 100%.

Intranasal drug administration

Intranasal drug delivery is a reliable method to bypass the blood–brain barrier and deliver a wide range of therapeutic agents, including small and large molecules, to the brain in both animals and humans, without increasing their concentrations in blood serum.[91] We have previously utilized this approach to promote white matter regeneration and functional recovery in mouse after neonatal hypoxia.[17] Sorafenib is a RAF kinase inhibitor and inhibits ATF5 transcription, and is clinically used for patients with several types of tumors.[51] To assess the effect of ATF5 inhibition on oRG, sorafenib was given intranasally to pigs. Sorafenib tosylate was dissolved with Dimethyl sulfoxide (DMSO) and then diluted with 45% polyethylene glycol 400, 5% Tween-80 and 55% saline at a concentration of 5 mg/mL. Animals were assigned to the vehicle (PBS) or sorafenib group. PBS or sorafenib was administered intranasally for 1 mL/kg. The pig was held, then administered with the drug solution using the intranasal mucosal atomization device with syringe (LMA MAD Nasal, Teleflex, Morrisville, NC) from nostril. The intranasal administration of Sorafenib was performed once per day for 6 days starting from 1 day post injury. We also performed intranasal delivery of salubrinal to assess ATF5 activation on oRG function in non-injured piglets and after neonatal ischemic injury. Salubrinal is eIF2α phosphatase inhibitor and induces ATF5 through eIF2a phosphorylation.[57] Injection of salubrinal into the brain increases ATF5 levels and promotes neuroprotection.[58] Salubrinal was dissolved with DMSO and then diluted with 45% polyethylene glycol 400, 5% Tween-80 and 55% saline at a concentration of 1 mg/mL. Pigs were assigned to the vehicle (PBS) or salubrinal group. PBS or salubrinal were administered intranasally at 1 mL/kg using the same method described above. To analyze the effect on oRG proliferation, the drug was administered to a 2-week-old piglet without brain injury once per day for 7 days. To assess the association between ATF5 activation, oligodendrogenesis and white matter regeneration, salubrinal was administered once per day from 8 to 14 days post injury.

SVZ cell sorting and nuclear isolation

Animals were anesthetized and transarterially perfused through the common carotid artery with 500 mL of cold saline, as previously described.[23] Brains were removed then transferred to vials with ice-cold Dulbecco's Modified Eagle's Medium (DMEM, Sigma). Brains were then cut into thick (1cm) coronal sections spanning the anterior part of the SVZ.[24] The SVZ was dissected in DMEM on ice and chopped into small pieces with micro forceps under a stereo microscope. Tissue was dissociated in 15 mL conical tubes with TrypLE Express Enzyme (GIBCO, Big Cabin, OK) for 30 min at 37°C with constant agitation. Following dissociation, TrypLE was inactivated with Hanks' Balanced Salt Solution (HBSS, Gibco). Tissue was centrifuged at 300g for 5 min at room temperature and resuspended in HBSS with 10% DNase (Worthington). After trituration with 10 mL pipette, we allowed any fragments/debris of undissociated tissue remaining after trituration to settle to the bottom of the tube. The cloudy cell suspension was transferred to 15 mL conical tubes and centrifuge at 300g for 5 min at room temperature. Cells were resuspended in PBS with 10% FBS (Invitrogen) then filtered through a 40 μm cell strainer (BD Biosciences). To assess cell viability, Trypan blue solution (Sigma) was added to a small fraction of the cell suspension and mix thoroughly. Numbers of total cells and stained non-viable cells were counted using the hemocytometer, then cell viability was determined. In all cases, cell viability was more than 98%.

Methods from Johnson and colleagues were used for isolating cells.[40] For cell surface staining, cells were stained with the indicated primary antibodies (mouse anti-GLAST-PE (1:50, Miltenyi Biotec), and rabbit anti-CD133 (1:100, abcam)), in 10% FBS in PBS for 30 min at 4°C, following by the Alexa Fluor 488 donkey anti-rabbit IgG secondary antibody (1:250) in 10% FBS in PBS for 30 min at 4°C. To remove dead cells, SYTOX Red Dead Cell Stain (Invitrogen) was used according to manufacturer's instructions. All fluorescence-activated cell sorting (FACS) analyses were performed on a BD LSR II or a Canto II Flow Cytometer, and data were analyzed with FlowJo software (Tree Star, Inc.). For isotype controls of CD133, cells were stained with the Alexa Fluor 488 donkey anti-rabbit IgG secondary antibody (1:250) in 10% FBS in PBS for 30 min at 4°C. Nuclear isolation was then performed according to the protocol of isolation of nuclei from the single cell suspension (10x Genomics). Briefly, the cell suspension was centrifuged at 300g for 5 min at room temperature, resuspended in 1 mL Lysis Buffer (10 mM Tris-HCl, 10 mM NaCl, 3 mM MgCl2, and 0.1% Nonidet P40 Substitute in Nuclease-Free Water), and then chilled on ice for 5 min. Nuclei were centrifuged at 300g for 5 min at 4°C and resuspended in 1 mL Nuclei Wash and Resuspension Buffer (1x PBS with 1.0% BSA and 0.2U/μL RNase Inhibitor) twice. After centrifugation at 300*g* for 5 min at 4°C, nuclei were resuspended in PBS, filtered through a 40 μm cell strainer (BD Biosciences), and stored at −80°C until further processing.

RNAseq library preparation and sequencing

RNA was isolated using the Absolutely RNA Nanoprep Kit (Agilent). RNA samples were sent to the Genome Sciences and Bioinformatics core at Penn State College of Medicine for library preparation and RNA-sequencing. RNA quality and quantity were determined using the Bioanalyzer Pico Kit (Agilent). The cDNA libraries were prepared using NuGEN's Ovation SoLo RNA-Seq System (Tecan Genomics, Inc.). This system offers a built-in Unique Molecular Identifier (UMI) application as well as a depletion of rRNA and other high-abundant transcripts using the proprietary AnyDeplete technology. UMIs are used to eliminate possible PCR duplicates in sequencing datasets and therefore facilitate unbiased gene expression profiling. The basic principle behind the UMI deduplication step is to collapse reads with identical mapping coordinates and UMI sequences. This step helps increase the accuracy of sequencing read counts for downstream analysis of gene expression levels. The processed libraries were assessed for size distribution and concentration using BioAnalyzer High Sensitivity DNA Kit (Agilent). The libraries were pooled and diluted to 3 nM using 10 mM Tris-HCl, pH 8.5 and then denatured using the Illumina protocol. The denatured libraries were loaded onto an S1 flow cell on an Illumina NovaSeq 6000 (Illumina) and run for 2X50 cycles according to the manufacturer's instructions. De-multiplexed and adapter-trimmed sequencing reads were generated using Illumina bcl2fastq (released version 2.18.0.12), allowing no mismatches in the index read. The FASTQ files were quality controlled using fastp (version 0.20.1).[79] The first 5 bases from the 5′ end of the forward read were trimmed according to the manufacturer's recommendation (Tecan). The transcript expression was quantified using Kallisto (version 0.46.2) based on the set of Sscrofa11.1 protein-coding cDNAs.[80] The transcript quantification was summarized to gene expression level using R package tximport (version 1.18.0).[81] Differential gene expression analysis was performed using default parameters with DeSeq2 package for R (iDEP, version 93).[77,78] The threshold for defining significant DEGs was an adjusted *p* value <0.1, with 1.4 of minimal fold change. The volcano plot and heatmaps were generated using iDEP. Enrichr was used for pathway analysis to identify cellular and molecular functions and the associated genes implicated from DEGs between oRG-injury and oRG-control groups, and vRG-injury and vRG-control groups.[41–43] Selected genes were then validated via RNAscope.

Primary glial cell culture and immunocytochemistry

The primary mixed glial cell culture was performed as described previously with some modifications.[92] Briefly, cerebral cortex tissues from ICR mouse pups at postnatal day 1 were dissociated using a papain dissociation system (Worthington Biochemical). The dissociated cells were plated on cover grasses coated with 50 μg/mL of poly-L-lysine (1×10^4 cells per well in 24-well plates), and cultured in KnockOut DMEM/F-12 (ThermoFisher) supplemented with 0.5% fetal bovine serum, 100 μg/mL of bovine serum albumin, 1x GlutaMAX (ThermoFisher), 1x *N*-2 supplement (ThermoFisher), 10 ng/mL of AA homodimeric form of platelet-derived growth factor (PDGF-AA, Fujifilm-Wako), 10 nM biotin (B4501, Merck), 30 ng/mL of thyronine (T2877, Merck), and 30 ng/mL of thyroxine (T2376, Merck) with 0, 4 or 40 μM salubrinal (Sigma-Aldrich) in humidified atmosphere of 8.5% CO2 in air at 37°C. For differentiation and proliferation assays, cells were fixed using 4% paraformaldehyde in PBS for 30 min at RT. After permeabilizing and blocking with 0.1% saponin and 1% normal goat serum in PBS, the cells were incubated with the primary antibodies overnight at 4°C. The binding of specific antibodies was detected with Alexa Fluor-conjugated secondary antibodies (1:1000, Invitrogen) along with Hoechst 33342 for nuclei labeling. The following primary antibodies were used: mouse anti-MBP (1: 200, sc-271524, Santa Cruz), rabbit anti-NG2 (1:200, ab275024, abcam). All images were acquired using an LSM 700 confocal laser-scanning microscope (Carl Zeiss, Jena, TH, Germany) with a 20× objective lens. The proportions of both MBP^+ and NG2^+ cells, and the ratio of MBP^+ cells to NG2^+ cells were measured using Fiji ImageJ software.

Behavioral tests

The piglets gait behavioral test was performed and adapted with modifications from previous studies.[93–95] Animals were subjected to gait assessment at 6 weeks (4 weeks post injury), using a GAITFour HD electronic, pressure-sensitive mat (7 × 0.85 m, CIR Systems Inc., Franklin, NJ). The active area is 6.10 × 0.61 m, and a grid, 23,040 sensors. The GAITFour HD mat was placed down the length of the chute. Metal grid panels were put on bilateral sides of the mat. Animals were trained to walk back and forth across the track at a consistent pace using food rewards. The gait record was collected as valid trials when the animal crossed the entire length of the mat at a consistent gait with less than 10% velocity variability, a minimum of four gait cycles, and no external distraction. The following spatial, temporal and pressure gait parameters were recorded.

(1) Spatial parameters.
  (a) Step Length: The length between the heel center of the current paw print to the heel center of the previous paw print on the opposite foot.
  (b) Stride Length: The length between the heel points of two consecutive paw prints of the same paw.
(2) Temporal parameters.
  (a) Stance time: The stance phase is the weight-bearing portion of each gait cycle. The stance time is elapsed between the first contact and the last contact of one identified paw.
  (b) % Stance time: The percentage of stance time compared to gait cycle.
  (c) Stride Time: The time elapsed between the first contacts of two consecutive paw strikes of the same paw.
  (d) Stride Velocity: The value obtained after dividing the Stride Length by the Stride Time.
(3) Pressure measurements.
  (a) Total Scale Pressure (TSP): The sum of peak pressure values recorded from each activated sensor by a paw during mat contact, represented by the switching levels and reported as a scaled pressure from 0 to 7 for each sensor.
  (b) Total pressure index as a percentage (TPI%): TSP expressed as a percentage of all four limbs. This demonstrates the percentage of weight distribution across all four paws.
  (c) GAIT4Dog Lameness Score (GLS): Score based on 100 for each leg. Above 100 indicates compensation, and less than 100 indicates insufficient limb function such as paralysis and pain during stance.

For each trial, a minimum of five gait cycles with less than 10% variability in velocity were selected. All gait parameters were calculated automatically using the GAITFour software. For each animal, the trials collected at every time point were averaged. Age-matched, normal pigs (without brain injury) underwent gait assessment at the same time point to brain injury animals.

DTI acquisition and processing

Magnetic resonance imaging (MRI) was performed on post-fixed 6-week-old piglet brains (4 weeks post injury). *Ex vivo* images were acquired at the Molecular Imaging Laboratory at Howard University (Washington, D.C.) using a Bruker 7.0T MRI machine (Bruker Corporation, Billerica, MA) and a 72 mm birdcage volume coil, with the brain placed in Fomblin-filled MR compatible plastic containers. Diffusion weighted images were acquired using a 3D spin echo sequence with TR 275ms, TE 31.7ms, Δ 20ms and δ 5ms, along 21 diffusion gradient directions with b-value of 1000 s/mm^2. A non-diffusion weighted image (b = 0) was also scanned. Transverse sections were planned parallel to the anterior commissure–posterior commissure line. The imaging matrix was 160 × 128 × 96 (field of view: 75 × 60 × 45 mm), with an isotropic voxel size of 0.468 × 0.468 × 0.468 mm^3 for the piglet brains, which covered the entire brain including cerebrum, brainstem and cerebellum without gaps. The total scan time per brain was approximately 13 h. All images were visually reviewed for artifacts due to subject motion and instrument malfunction, and any images with identified artifacts were retaken. DTI datasets were preprocessed using the Tolerably Obsessive Registration and Tensor Optimization Indolent

Software Ensemble (TORTOISE) software package (NIH, Bethesda, MD), and corrected for motion-related misalignment caused by frequency drifts, with appropriate rotations to the b-matrix. Fractional anisotropy (FA), axial diffusivity (AD), mean diffusivity (MD), and radial diffusivity (RD) maps were then generated from the corrected diffusion imaging datasets using DTI Studio (Center for Brain Imaging Science, Johns Hopkins University, Baltimore, MD). The DTI maps were analyzed based on a homebuilt piglet brain atlas that can segment up to 133 brain regions. The piglet brain atlas was registered to individual brain images using DTI Studio to obtain region-specific DTI indices, including FA, AD, MD, and RD. ROIs of cortical white matter were obtained by further separating cortical ROIs into cortical gray matter and superficial white matter regions by expert-defined FA thresholding for each individual brain using ROIEditor (Center for Brain Imaging Science, Johns Hopkins University, Baltimore, MD). Thresholding value ranged from 0.2 to 0.3 as an average value for each individual brain.

Experimental design

The number of human brains, piglets, cells, and experimental replication can be found in the respective figure legend. No specific strategy for randomization was employed, and no blinding was used. No statistical calculation was used to estimate the sample size. Sample sizes for experiments were determined according to previous studies.[23,24] We included piglets with ischemic lesions in dorsal PVWM in the analyses.

QUANTIFICATION AND STATISTICAL ANALYSIS

GraphPad Prism 10 software was used for statistical tests. All data are shown as the mean ± SEM (standard error of the mean). A Shapiro-Wilk test was used to assess normal distribution of data. Parametric and non-parametric methods were applied based on the results obtained from the normality test. Two groups were compared using a two-tailed unpaired t test and Mann-Whitney U-test. Multiple group comparisons were performed by one-way and two-way ANOVA followed by Tukey or Sidak's multiple comparison tests, or by Kruskal-Wallis test. The correlation between ages and densities of *Hopx*$^+$ cells was analyzed by Pearson's correlation test. A *P*-value less than 0.05 was considered to be statistically significant. All statistical data, including the statistical tests used, mean ± SEM, and *p* values are indicated in the text, figure legends, figures, STAR Methods, and Supplemental tables. Biological replicates are indicated in figure legends.